JOURNAL OF PETROLOGY

Journal of Petrology, 2019, Vol. 60, No. 9, 1753–1772
doi: 10.1093/petrology/egz047
Advance Access Publication Date: 5 November 2019
Original Article

OXFORD

Pacific Lithosphere Evolution Inferred from Aitutaki Mantle Xenoliths

Eric Snortum[1], James M. D. Day [1]* and Matthew G. Jackson[1,2]

[1]Scripps Institution of Oceanography, University of California San Diego, La Jolla, CA 92093-0244, USA; [2]Department of Earth Science, University of California Santa Barbara, Santa Barbara, CA 93106, USA

*Corresponding author. E-mail: jmdday@ucsd.edu

Received April 30, 2019; Accepted October 29, 2019

ABSTRACT

Highly siderophile element (HSE: Os, Ir, Ru, Pt, Pd, Re), major and trace element abundances, and ^{187}Re–^{187}Os systematics are reported for xenoliths and lavas from Aitutaki (Cook Islands), to investigate the composition of Pacific lithosphere. The xenolith suite comprises spinel-bearing lherzolites, dunite, and harzburgite, along with olivine websterite and pyroxenite. The xenoliths are hosted within nephelinite and alkali basalt volcanic rocks ($^{187}Os/^{188}Os$ ~0·1363 ± 13; 2SD; Σ_{HSE} = 3–4 ppb). The volcanic host rocks are low-degree (2–5%) partial melts from the garnet stability field and an enriched mantle (EM) source. Pyroxenites have similar HSE abundances and Os isotope compositions (Al_2O_3 = 5·7–8·3 wt %; Σ_{HSE} = 2–4 ppb; $^{187}Os/^{187}Os$ = 0·1263–0·1469) to the lavas. The pyroxenite and olivine websterite xenoliths directly formed from—or experienced extensive melt–rock interaction with—melts similar in composition to the volcanic rocks that host the xenoliths. Conversely, the Aitutaki lherzolites, harzburgites and dunites are similar in composition to abyssal peridotites with respect to their $^{187}Os/^{188}Os$ ratios (0·1264 ± 82), total HSE abundances (Σ_{HSE} = 8–28 ppb) and major element abundances, forsterite contents ($Fo_{89·9\pm1·2}$), and estimated extents of melt depletion (<10 to >15%). These peridotites are interpreted to sample relatively shallow Pacific mantle lithosphere that experienced limited melt–rock reaction and melting during ridge processes at ~90 Ma. A survey of maximum time of rhenium depletion ages of Pacific mantle lithosphere from the Cook (Aitutaki ~1·5 Ga), Austral (Tubuai'i ~1·8 Ga), Samoan (Savai'i ~1·5 Ga) and Hawaiian (Oa'hu ~2 Ga) island groups shows that Mesoproterozoic to Neoproterozoic depletion ages are preserved in the xenolith suites. The variable timing and extent of mantle depletion preserved by the peridotites is, in some instances, superimposed by extensive and recent melt depletion as well as melt refertilization. Collectively, Pacific Ocean island mantle xenolith suites have similar distributions and variations of $^{187}Os/^{188}Os$ and HSE abundances to global abyssal peridotites. These observations indicate that Pacific mantle lithosphere is typical of oceanic lithosphere in general, and that this lithosphere is composed of peridotites that have experienced both recent melt depletion at ridges and prior and sometimes extensive melt depletion across several Wilson cycles spanning periods in excess of two billion years.

Key words: Aitutaki; Pacific; mantle; Os isotopes; highly siderophile elements; melt metasomatism

INTRODUCTION

The composition of Earth's mantle is a key parameter for understanding processes in terrestrial evolution, including the total heat budget, as well as the surficial expression of the outermost layer of Earth—the lithosphere—and its physical properties. Large-scale effects, including response to physical stress and buoyancy, have been attributed to relatively minor variations in chemical composition within the mantle (e.g. Karato, 1986; Hirth & Kohlstedt, 1996; Afonso *et al.*, 2007; Simon *et al.*, 2008; Day *et al.*, 2019). Lithospheric mantle composition is also likely to be important owing to its

© The Author(s) 2019. Published by Oxford University Press. All rights reserved. For permissions, please e-mail: journals.permissions@oup.com

Downloaded from https://academic.oup.com/petrology/article/60/9/1753/5613188 by UCSD-Philosophy user on 11 July 2024

role in generation of melts at the lithosphere–asthenosphere boundary, as a direct source of melts, and ultimately, its role in subduction zone recycling (e.g. Zindler & Hart, 1986). Contributing to our understanding of the oceanic mantle lithosphere are abyssal peridotites found at mid-ocean ridges and fracture zones (e.g. Warren, 2016), ophiolites (e.g. O'Driscoll *et al.*, 2012), and mantle xenoliths found at ocean islands (e.g. Simon *et al.*, 2008). Ocean islands allow the opportunity for insight into mantle compositions from xenoliths brought to the surface by their host volcanic rocks. During ascent to the surface, these melts can react with the original mantle peridotite at depth and obviously—or subtly—affect the composition of the xenolith suite (e.g. Kelemen *et al.*, 1992). It has been demonstrated that melt–rock reaction can fundamentally change the composition of basalts forming at mid-ocean ridges (Lissenberg & Dick, 2008), and results in significant structural modification to young lithosphere (Day *et al.*, 2019).

Studies of abyssal peridotites have shown that the oceanic crust can be underlain by extensively melt-depleted peridotite (e.g. Johnson *et al.*, 1990; Harvey *et al.*, 2006), yet the degree, timing and extent of depletion, and whether this occurs across entire ocean basins remain unconstrained. From limited abyssal peridotite data, it appears that the Pacific plate is relatively homogeneous but can contain both old depleted and young enriched mantle domains (Lassiter *et al.*, 2014; Day *et al.*, 2017). The ability to sample the Pacific oceanic lithosphere is limited by fast spreading (half-plate speed ~4–10 cm a^{-1}; e.g. Müller *et al.*, 2008), leading to few exposures at transform faults, and the absence of large tectonic features that can be sampled for abyssal peridotites, such as mega-mullions, as is the case for slower spreading oceanic plates (e.g. Arctic, Atlantic and Indian Ocean basins). Convection times of upper mantle materials through one cycle are of the order of 240–400 Myr (Donnelly *et al.*, 2004; Zhong & Zhang, 2005), and it has been shown that over multiple mantle convection cycles strongly depleted peridotite can remain relatively undisturbed and may even cluster to form larger heterogeneities within the mantle (Manga, 1996). These lines of evidence suggest that the oceanic crust could sit atop large areas of strongly depleted (up to 20% melt depleted relative to primitive mantle) upper mantle.

The alternative view to abyssal peridotites for understanding the structure and composition of oceanic lithosphere is to use mantle xenolith suites erupted at ocean islands. Several Pacific Ocean island chains, including Hawaii, Samoa, the Austral Islands, and the Cook Islands, are hosts to mantle xenolith suites (e.g. White, 1966; Wood, 1978; Fodor *et al.*, 1982; Wright, 1987; Hauri *et al.*, 1993). Here we investigate a xenolith suite and associated lavas from Aitutaki, in the Cook Islands. Aitutaki occurs on the SW Pacific plate at the NW extremity of the Cook–Austral hotspot track (Fig. 1). We report data for spinel lherzolites, harzburgites and dunites (collectively termed 'peridotites'), and mafic pyroxenites and one olivine websterite (termed 'pyroxenites'). The Aitutaki peridotite and pyroxenite xenolith suite offers the opportunity to investigate oceanic mantle in a poorly sampled region of the SW Pacific, with the nearest studied mantle xenoliths being over 1200 km distant at Tubuai (Austral Islands) to the SE, and ~1500 km distant at Savaii (Samoa) to the NW. We use these samples to examine the nature and extent of melt–rock reaction between lithosphere and intraplate plate melts. We then consider the degree, timing and extent of melt depletion in the Pacific lithosphere and compare our findings with global abyssal peridotites to assess the gross geochemical structure of oceanic lithosphere evident from Pacific oceanic island xenolith suites.

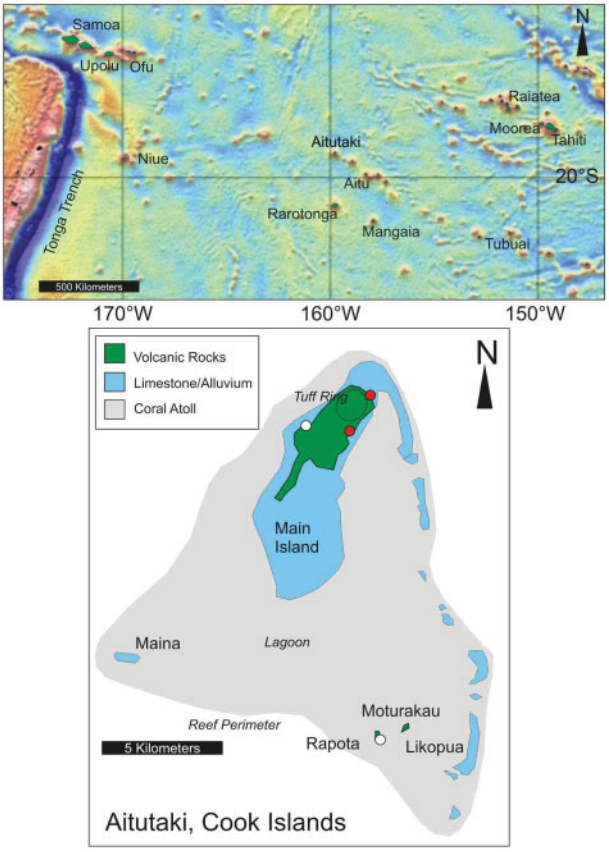

Fig. 1. Location of Aitutaki in the wider southwestern Pacific region shown on a marine gravity anomaly map after Sandwell & Smith (2009) and https://topex.ucsd.edu/marine_grav/mar_grav.html, and geology of the island based on Wood (1978). Mantle xenoliths have been examined from Aitutaki (this study; red dots show xenolith sampling locations), as well as Savaii (Samoa) and Tubuai for Re–Os isotope systematics (Jackson *et al.*, 2016). White dots show sampling locations for lavas AK1020 and AK1025.

METHODS

Mineral chemical analyses and imaging

Two polished thin-sections (AK1023A and B) were examined to determine the relationship and compositions of spinel and orthopyroxene using a Zeiss EVO 50

Downloaded from https://academic.oup.com/petrology/article/60/9/1753/5613188 by UCSD-Philosophy user on 11 July 2024

scanning electron microscope equipped with an Oxford Instruments energy-dispersive spectrometer (EDS) at Harvard University, details of which are provided in the Supplementary Data (available for downloading at http://www.petrology.oxfordjournals.org). Back-scattered electron images were obtained and semi-quantitative mineral determinations were carried out with an acceleration potential of 15 keV, with a resolution of 5 nm.

Mineral major and minor element analyses were performed on polished 1 inch rounds containing olivine and orthopyroxene grains from Aitutaki xenolith samples. Measurements were made using a JEOL JXA-8900 electron microprobe analyzer at the University of Maryland. Mineral compositions were determined in wavelength-dispersive spectral mode using an acceleration potential of 15 keV and a 20 nA beam current, with the beam focused to 2 μm peak; background counting times were 20–30 s and standard ZAF correction procedures were used. The detection limits (3σ above background) are <0·03 wt % for all oxides listed. Operating conditions for analysis included peak and background times for Ni, Cr, Ca, and Fe of 30·5 s, and for Ti, Mn, Al, Mg, and Si of 20·5 s. Primary standards used for analyses were as follows: San Carlos Olivine (Fe, Mg, Si, and Ni), Bushveld chromite (Cr), ilmenite (Mn), and Kakanui hornblende (Ca, Al, and Si). Statistical uncertainties (2σ) resulting from counting statistics were 1·5% for FeO, 0·5% for MgO, 23% for MnO, 13% for NiO and 0·7% for SiO_2. Concentrations for CaO, TiO_2, Cr_2O_3, and Al_2O_3 were generally below detection limits.

Whole-rock major and trace element abundance analyses

Major element compositions were measured by X-ray fluorescence (XRF) at Franklin and Marshall College using a PW 2404 PANalytical XRF vacuum spectrometer following the procedures outlined by Boyd & Mertzman (1987). Major element analyses by XRF involved standard lithium tetraborate fusion techniques using 3·6:0·4 g $LiBO_4$:sample powder. Ferrous iron concentrations were determined by titration with potassium dichromate. Precision is estimated using repeat analyses of a range of USGS standards, with long-term reproducibility (in wt % and 2σ absolute standard deviation, $n = 13$) of ±0·13 for SiO_2, ±0·01 for TiO_2, ±0·09 for Al_2O_3, ±0·63 for FeO, ±0·47 for Fe_2O_3, ±0·10 for $Fe_2O_3^T$, ±0·01 for MnO, ±0·04 for MgO, ±0·07 for CaO, ±0·03 for Na_2O, ±0·01 for K_2O, and ±<0·01 for P_2O_5. Accuracy for the average of 13 runs of BHVO-2 relative to USGS values is better than 0·2% for SiO_2 and TiO_2, <1% for Al_2O_3, MgO, Fe_2O_3T, CaO, Na_2O and P_2O_5, and <3% for K_2O (see Day *et al.*, 2017, for details).

Trace element abundances were determined at the Scripps Isotope Geochemistry Laboratory (SIGL), Scripps Institution of Oceanography, using methods described previously (Day *et al.*, 2014). One hundred milligrams of powder were precisely weighed and digested in a 1:4 mixture of Teflon–distilled HNO_3:HF for >72 h at 150°C on a hotplate. Rock standards (BHVO-2, BIR-1, HARZ-01) and total procedural blanks were prepared with samples. After drying down and sequential HNO_3 dry-down steps to break down fluorides, clear sample solutions, free of any solid material, were diluted by a factor of 5000 in 2% HNO_3 and doped with a 1 ppb In solution to monitor instrumental drift. Solutions were measured by inductively coupled plasma mass spectrometry (ICP-MS) using a Thermo Scientific iCAPQc quadrupole ICP-MS system at the SIGL. Reproducibility of the reference materials was generally better than 5% (RSD) for basaltic and peridotite standards, and element abundances were generally within error of recommended values. Elemental V, Ti, Mn, Sr, Rb, Zr and Cr were measured by both XRF and ICP-MS techniques, yielding generally 1:1 correlation (see Table 1). Nonetheless, we prefer the data from ICP-MS for most of these elements owing to the higher sensitivity of this technique.

Highly siderophile element abundances and $^{187}Os/^{188}Os$ ratios

Osmium isotope and highly siderophile element (HSE) abundance analyses were performed at the SIGL. One gram of homogenized powder was precisely weighted before digestion in sealed borosilicate Carius tubes with isotopically enriched multi-element spikes (^{99}Ru, ^{106}Pd, ^{185}Re, ^{190}Os, ^{191}Ir, ^{194}Pt), and 12 ml of a 1:2 mixture of multiply Teflon distilled HCl and HNO_3 purged of excess Os by repeated treatment and reaction with H_2O_2. Samples were digested to a maximum temperature of 270°C in an oven for 72 h. Osmium was triply extracted from the acid using CCl_4 and then back-extracted into HBr (Cohen & Waters, 1996), prior to purification by micro-distillation (Birck *et al.*, 1997). Rhenium and the other HSE were recovered and purified from the residual solutions using standard anion exchange separation techniques (Day *et al.*, 2016).

Isotopic compositions of Os were measured by thermal ionization mass spectrometry (TIMS) in negative-ion mode using a ThermoScientific Triton system in peak-jumping mode on the secondary electron multiplier. Rhenium, Pd, Pt, Ru and Ir were measured using a Cetac Aridus II desolvating nebulizer coupled to a ThermoScientific iCAPQc ICP-MS system. Offline corrections for Os involved an oxide correction, an iterative fractionation correction using $^{192}Os/^{188}Os = 3{\cdot}08271$ and assuming the exponential law, a ^{190}Os spike subtraction, and an Os blank subtraction. Precision for $^{187}Os/^{188}Os$, determined by repeated measurement of the UMCP Johnson–Matthey standard was better than ±0·2% (2SD; 0·11374 ± 8; $n = 6$). Rhenium, Ir, Pt, Pd and Ru isotopic ratios for sample solutions were corrected for mass fractionation using the deviation of the standard average run on the day over the natural ratio for the element. External reproducibility for HSE analyses was better than 0·5% for 0·5 ppb solutions and all reported

Downloaded from https://academic.oup.com/petrology/article/60/9/1753/5613188 by UCSD-Philosophy user on 11 July 2024

Table 1: Major and trace element abundance data for Aitutaki xenolith and lavas

Sample:	AK1008	AK1027	AK1021	AK1023-5	AK1017	AK1023-4	AK1006	AK1023-7	AK1005	AK1023B
Lithology:	Dunite	Harzburgite	Lherzo	Lherzo	Lherzo	Lherzo	Lherzo	Lherzo	Lherzo	Lherzo
XRF (wt %)										
SiO_2	40·9	43·2	43·1	42·0	43·6	40·6	43·6	42·3	44·9	44·2
TiO_2	0·01	0·08	0·07	0·19	0·12	0·16	0·16	0·17	0·03	0·20
Al_2O_3	0·26	1·52	3·23	2·32	3·00	2·08	2·98	2·24	3·57	4·43
$Fe_2O_3^T$	11·2	10·4	10·5	12·6	9·4	14·7	10·0	13·5	8·5	10·8
MnO	0·18	0·15	0·134	0·167	0·131	0·195	0·129	0·170	0·13	0·155
MgO	46·7	41·8	41·2	40·3	40·1	39·8	39·3	38·2	38·1	36·6
CaO	0·24	2·08	0·95	1·55	2·40	1·45	3·05	2·67	3·75	2·40
Na_2O	0·06	0·12	0·09	0·21	0·61	0·20	0·42	0·19	0·15	0·39
K_2O	<0·001	0·001	0·001	0·152	0·297	0·118	0·082	0·087	0·103	0·221
P_2O_5	0·016	0·017	0·015	0·032	0·027	0·047	0·009	0·071	0·006	0·058
Total	99·60	99·31	99·26	99·55	99·73	99·30	99·63	99·55	99·21	99·43
LOI	0·38	0·58	0·88	1·12	1·27	1·36	0·83	1·47	0·32	1·29
XRF (ppm)										
Rb	<2	<2	<2	<2	<2	<2	<2	<2	<2	<2
Sr	10	23	13	17	48	32	42	37	37	74
Zr	4	6	2	1	11	6	6	8	5	13
V	9	59	64	86	71	88	80	96	91	78
Cr	254	2690	2990	3172	2024	4175	2153	3442	3780	2031
ICP-MS (ppm)										
Li	2·0	0·4	0·7	2·2	9·7	6·3	2·8	9·4	1·4	2·0
B	0·6	0·2	0·2	0·3	0·5	0·5	0·4	0·3	0·5	0·4
Sc	2·0	6·1	5·9	9·0	10·3	8·3	7·8	13·2	16·3	8·3
Ti	176	566	454	1102	807	909	996	1043	316	1205
V	5·6	52·5	44·2	62·9	58·1	62·1	66·6	75·5	76·6	65·7
Cr	177	2645	2331	2724	1747	3391	1617	3074	2207	1698
Mn	980	765	784	930	850	1172	753	1118	793	942
Co	133·0	96·2	97·0	104·2	96·7	123·5	98·1	110·6	79·5	95·0
Ni	2416	1809	1927	1898	1918	1762	1968	1406	1513	1575
Cu	5·7	34·3	7·7	14·9	9·5	18·3	12·4	37·3	15·4	15·1
Zn	46·1	44·2	49·9	57·2	44·8	77·1	44·4	81·2	32·5	43·1
Ga	1·68	1·87	3·09	3·68	5·01	4·05	3·63	4·05	2·47	4·16
Ge	0·99	0·75	0·85	0·92	0·83	1·03	0·85	1·03	0·74	0·91
Rb	0·81	1·15	0·78	6·95	20·06	5·37	19·27	5·54	9·17	6·06
Sr	9·58	20·5	12·6	31·5	58·1	46·9	43·9	58·8	53·4	73·7
Y	0·20	0·85	1·08	1·66	2·85	1·92	1·72	2·06	2·03	3·46
Zr	1·08	5·09	3·33	7·65	9·47	10·88	9·11	12·26	0·30	11·99
Nb	0·37	1·67	0·88	1·89	3·49	3·03	0·82	3·47	0·27	5·28
Mo	0·04	0·06	0·03	0·31	0·09	0·23	0·20	0·83	0·08	0·33
Sn	0·24	0·33	0·82	0·27	0·29	0·26	0·33	0·29	0·22	0·25
Cs	0·04	0·05	0·03	0·11	6·94	0·15	3·81	0·11	1·32	0·04
Ba	5·28	9·85	9·69	28·8	207	44·1	29·8	50·6	9·00	47·7
La	0·35	1·41	0·94	1·59	2·60	2·92	1·06	4·79	0·59	4·23
Ce	0·63	3·05	1·22	3·95	4·85	6·07	2·07	8·27	0·79	7·45
Pr	0·07	0·36	0·19	0·42	0·52	0·70	0·33	0·94	0·09	0·79
Nd	0·26	1·45	0·79	1·76	2·08	2·74	1·54	3·80	0·36	3·06
Sm	0·05	0·32	0·18	0·43	0·47	0·61	0·40	0·82	0·10	0·64
Eu	0·02	0·10	0·07	0·15	0·20	0·21	0·14	0·27	0·04	0·23
Gd	0·05	0·31	0·21	0·44	0·54	0·61	0·43	0·80	0·18	0·73
Tb	0·01	0·04	0·03	0·07	0·08	0·09	0·06	0·10	0·04	0·11
Dy	0·04	0·21	0·20	0·39	0·52	0·49	0·38	0·51	0·31	0·68
Ho	0·01	0·04	0·04	0·07	0·11	0·09	0·07	0·09	0·07	0·13
Er	0·02	0·09	0·12	0·19	0·31	0·23	0·17	0·22	0·24	0·38
Tm	0·004	0·01	0·02	0·03	0·04	0·03	0·02	0·03	0·04	0·05
Yb	0·02	0·08	0·13	0·18	0·29	0·21	0·13	0·16	0·26	0·35
Lu	0·00	0·01	0·02	0·03	0·04	0·03	0·02	0·02	0·04	0·05
Hf	0·03	0·13	0·10	0·24	0·23	0·29	0·23	0·38	0·03	0·30
Ta	0·02	0·08	0·05	0·07	0·23	0·13	0·10	0·15	0·01	0·25
W	0·02	0·12	0·07	0·49	0·11	0·86	0·60	0·72	0·10	0·37
Pb	0·23	0·28	0·09	0·59	1·66	1·97	0·49	2·31	0·46	0·59
Th	0·03	0·15	0·11	0·15	0·46	0·29	0·04	0·74	0·08	0·56
U	0·06	0·06	0·03	0·09	0·16	0·16	0·03	0·20	0·05	0·19

(continued)

Downloaded from https://academic.oup.com/petrology/article/60/9/1753/5613188 by UCSD-Philosophy user on 11 July 2024

Table 1: Continued

Sample:	AK1023-8	AK1023A	AK1023-6	AK1023-1	AK1028	AK1023-2	AK1029	AK1023-3	AK1026	AK1025
Lithology:	Lherzo	Lherzo	Lherzo	Lherzo	Websterite	Pyroxenite	Pyroxenite	Pyroxenite	Pyroxenite	Basanite
XRF (wt %)										
SiO_2	43·6	44·3	42·9	43·1	45·6	46·5	49·6	47·0	47·3	44·5
TiO_2	0·11	0·20	0·22	0·39	0·41	0·62	0·58	0·80	0·99	2·03
Al_2O_3	3·62	4·53	2·35	3·58	8·91	5·75	5·49	7·46	8·31	9·40
$Fe_2O_3^T$	12·0	10·5	12·9	14·2	9·4	11·6	10·2	9·5	8·5	12·9
MnO	0·17	0·149	0·148	0·170	0·19	0·181	0·18	0·150	0·13	0·18
MgO	36·4	35·6	35·3	30·8	28·6	22·8	21·2	18·7	14·6	15·5
CaO	2·99	3·46	5·68	6·88	5·75	11·39	11·37	15·32	18·78	13·35
Na_2O	0·21	0·49	0·28	0·43	0·44	0·55	0·63	0·69	1·18	1·22
K_2O	0·054	0·025	0·059	0·137	0·001	0·169	0·003	0·103	0·022	0·387
P_2O_5	0·058	0·047	0·017	0·034	0·032	0·017	0·032	0·023	0·019	0·262
Total	99·22	99·33	99·76	99·65	99·29	99·54	99·34	99·73	99·82	99·84
LOI	1·99	1·51	0·37	1·53	0·92	4·06	1·02	2·74	0·99	2·30
XRF (ppm)										
Rb	<2	<2	<2	<2	<2	<2	<2	<2	<2	9
Sr	37	56	10	25	26	51	53	22	93	419
Zr	5	9	3	6	16	13	9	16	23	120
V	120	85	120	157	150	176	194	247	306	270
Cr	2888	2484	1402	2703	4078	1712	2367	1475	559	1087
ICP-MS (ppm)										
Li	3·3	3·9	3·9	5·4	2·0	9·6	2·0	6·3	3·6	9·6
B	0·3	0·4	0·3	0·3	0·3	0·5	0·3	0·4	0·3	1·8
Sc	15·8	15·9	19·4	25·4	19·5	47·8	34·1	43·6	56·5	45·2
Ti	741	1255	1356	2291	2382	3620	3558	4890	6582	12241
V	96·1	75·5	93·6	131·5	141·5	155·4	198·4	246·1	355·7	276·0
Cr	2619	2276	1171	2263	3544	1649	2397	1278	643	1150
Mn	1077	1008	932	1177	1100	1163	1299	1006	1030	1318
Co	108·9	95·7	104·9	102·3	72·1	78·8	63·6	60·4	43·5	70·1
Ni	1666	1557	1378	1106	997	849	560	471	230	354
Cu	24·9	16·2	30·8	35·7	12·0	79·8	42·5	45·2	29·2	76·8
Zn	51·8	41·2	54·0	78·9	58·5	54·8	55·5	45·7	49·0	91·8
Ga	4·25	4·07	3·19	6·04	9·91	9·25	9·06	9·95	15·7	15·5
Ge	0·98	0·91	1·05	1·15	0·95	1·12	1·19	1·10	1·22	1·57
Rb	4·84	9·79	2·91	5·07	0·68	9·44	0·86	3·44	1·40	13·6
Sr	46·1	78·0	32·1	61·9	55·3	97·0	97·7	68·3	105	508
Y	3·43	5·37	3·24	5·07	6·61	8·07	7·28	10·4	13·0	19·7
Zr	6·98	12·21	6·79	13·48	19·50	20·27	19·71	25·14	35·04	130·5
Nb	3·69	5·15	0·99	1·32	3·93	1·97	3·92	2·11	1·81	27·45
Mo	0·17	0·29	0·26	0·28	0·11	0·13	0·08	0·82	0·06	0·85
Sn	0·24	0·29	0·32	0·35	0·38	0·51	0·49	0·60	1·00	1·13
Cs	0·08	0·13	0·04	0·18	0·03	0·11	0·03	0·05	0·05	0·38
Ba	41·8	55·9	12·9	30·0	66·0	63·8	46·4	42·1	56·0	184
La	3·86	4·52	1·24	3·04	4·01	4·27	5·28	4·69	4·15	22·2
Ce	7·18	8·05	2·99	5·86	8·05	12·90	13·45	9·49	10·71	46·8
Pr	0·81	0·87	0·41	0·85	1·02	1·41	1·66	1·61	1·97	5·82
Nd	3·06	3·27	1·96	3·79	4·47	6·63	6·91	7·89	11·00	23·9
Sm	0·65	0·74	0·58	1·06	1·22	1·80	1·72	2·26	3·64	5·04
Eu	0·24	0·26	0·21	0·38	0·45	0·62	0·60	0·81	1·26	1·67
Gd	0·74	0·90	0·67	1·17	1·39	1·99	1·90	2·45	3·86	5·23
Tb	0·11	0·15	0·11	0·19	0·22	0·30	0·28	0·39	0·56	0·71
Dy	0·73	0·96	0·67	1·11	1·33	1·80	1·62	2·34	3·12	4·09
Ho	0·14	0·21	0·12	0·21	0·26	0·32	0·29	0·43	0·52	0·73
Er	0·41	0·59	0·32	0·54	0·67	0·82	0·71	1·08	1·21	1·93
Tm	0·06	0·09	0·04	0·07	0·09	0·10	0·09	0·14	0·15	0·25
Yb	0·41	0·56	0·25	0·47	0·59	0·63	0·56	0·81	0·83	1·55
Lu	0·06	0·08	0·04	0·07	0·09	0·09	0·07	0·11	0·11	0·22
Hf	0·18	0·33	0·27	0·53	0·56	0·81	0·77	1·14	1·81	3·50
Ta	0·15	0·25	0·05	0·05	0·23	0·09	0·17	0·12	0·10	1·77
W	1·01	0·28	0·14	0·69	0·10	0·81	0·13	0·70	0·08	0·30
Pb	1·06	0·65	1·01	1·11	0·69	5·93	1·06	1·11	0·95	1·72
Th	0·69	0·84	0·14	0·30	0·54	0·29	0·61	0·52	0·29	2·80
U	0·17	0·19	0·05	0·12	0·08	0·15	0·10	0·13	0·05	0·63

(continued)

Downloaded from https://academic.oup.com/petrology/article/60/9/1753/5613188 by UCSD-Philosophy user on 11 July 2024

Table 1: Continued

Sample:	AK1017L	AK1020	BHVO-2	SD	RSD %	BIR-1a	SD	RSD %	HARZ-01	SD	RSD %	TAB
Lithology:	Nephelinite	Alkali basalt	$n=8$			$n=2$			$n=3$			$n=2$
XRF (wt %)												
SiO_2	39·0	45·7										
TiO_2	2·78	2·04										
Al_2O_3	11·72	11·27										
$Fe_2O_3^T$	15·3	12·5										
MnO	0·231	0·195										
MgO	11·3	14·8										
CaO	12·07	10·19										
Na_2O	4·85	2·01										
K_2O	1·244	0·560										
P_2O_5	1·195	0·692										
Total	99·70	99·88										
LOI	2·70	4·07										
XRF (ppm)												
Rb	51	19										
Sr	1389	798										
Zr	227	161										
V	204	200										
Cr	418	1076										
ICP-MS (ppm)												
Li	18·4	11·6	4·8	0·3	7	3·1	0·2	8	0·345	0·021	6	0·0001
B	1·9	1·8	1·0	0·1	7	0·3	0·0	3	1·838	0·117	6	0·0774
Sc	20·7	24·0	32·0	2·2	7	40·5	2·7	7	3·965	0·575	14	0·3962
Ti	16928	11720	16300	962	6	5747	412	7	12·97	1·85	14	0·0020
V	188·1	159·8	317·0	19·6	6	330	21	6	33·6	2·2	6	0·0471
Cr	202	739	280·0	17·1	6	381	26	7	2871	219	8	0·0020
Mn	1777	1349	1320·0	71·7	5	1357	80	6	798	73	9	0·0020
Co	62·7	67·3	45·0	2·7	6	54·3	3·9	7	107	8	7	0·0020
Ni	167	565	119·0	6·8	6	176	11	6	2350	152	6	0·0020
Cu	47·5	41·8	127·0	6·7	5	118·8	6·8	6	4·25	0·47	11	0·0002
Zn	151·0	107·1	103·0	2·6	3	67·8	2·4	4	53·3	4·1	8	1·2786
Ga	23·26	18·9	22·0	0·8	3	15·9	0·7	4	0·446	0·024	5	0·0006
Ge	2·51	1·66	1·6	0·1	5	1·2	0·1	4	0·865	0·073	8	0·0008
Rb	105·0	53·9	9·1	0·7	7	0·1	0·0	1	0·038	0·019	51	0·0002
Sr	1845	922	396·0	22·1	6	107·0	2·8	3	0·027	0·023	85	0·0002
Y	36·13	24·6	26·0	1·0	4	15·8	0·8	5	0·028	0·016	58	0·0002
Zr	249·8	155·6	172·0	6·1	4	15·3	0·5	4	0·649	0·043	7	0·0029
Nb	117·9	52·38	18·100	0·773	4	0·547	0·023	4	0·005	0·005	101	0·0002
Mo	4·74	1·08	4·000	0·209	5	0·066	0·006	9	0·134	0·008	6	0·0002
Sn	1·84	1·52	1·700	0·083	5	1·155	0·051	4	0·284	0·060	21	0·2377
Cs	5·14	4·15	0·100	0·013	13	0·003	0·000	17	0·125	0·028	23	0·0001
Ba	1048	659	131·000	2·995	2	7·083	0·044	1	0·346	0·210	61	0·0757
La	117·8	48·6	15·200	0·362	2	0·642	0·006	1	0·032	0·007	22	0·0002
Ce	212·4	82·1	37·500	0·772	2	2·010	0·079	4	0·443	0·021	5	0·0002
Pr	21·78	9·25	5·350	0·083	2	0·380	0·011	3	2·432	0·189	8	0·0002
Nd	79·01	37·6	24·500	0·306	1	2·443	0·049	2	0·219	0·042	19	0·0002
Sm	15·35	7·83	6·070	0·111	2	1·110	0·038	3	0·002	0·002	111	0·0002
Eu	4·71	2·71	2·070	0·029	1	0·527	0·004	1	0·001	0·001	154	0·0002
Gd	14·97	7·88	6·240	0·102	2	1·693	0·038	2	0·239	0·020	8	0·0002
Tb	1·72	1·01	0·920	0·013	1	0·343	0·003	1	0·0009	0·0003	34	0·0002
Dy	8·31	5·25	5·310	0·062	1	2·597	0·008	0	0·003	0·002	77	0·0002
Ho	1·34	0·90	0·980	0·016	2	0·568	0·010	2	0·0010	0·0004	46	0·0002
Er	3·14	2·24	2·540	0·029	1	1·693	0·006	0	0·241	0·024	10	0·0002
Tm	0·36	0·26	0·330	0·006	2	0·249	0·003	1	0·0011	0·0002	17	0·00002
Yb	1·94	1·58	2·000	0·029	1	1·608	0·006	0	0·011	0·001	7	0·0002
Lu	0·25	0·21	0·274	0·006	2	0·244	0·002	1	0·0025	0·0002	8	0·00002
Hf	5·63	3·72	4·360	0·072	2	0·586	0·010	2	0·017	0·001	7	0·0006
Ta	5·98	2·85	1·140	0·019	2	0·0432	0·0003	1	0·003	0·001	21	0·00002
W	0·94	0·86	0·210	0·003	2	0·0192	0·0003	2	6·500	0·222	3	0·0011
Pb	11·43	4·39	1·600	0·135	8	5·292	0·040	1	189	20	11	0·0002
Th	20·82	8·28	1·220	0·034	3	0·0328	0·0001	0	0·0016	0·0002	10	0·0002
U	3·71	1·48	0·403	0·010	3	0·0095	0·0001	1	0·0007	0·0001	11	0·00004

Downloaded from https://academic.oup.com/petrology/article/60/9/1753/5613188 by UCSD-Philosophy user on 11 July 2024

values are blank corrected. The total procedural blanks ($n = 2$) run with the samples gave $^{187}Os/^{188}Os = 0{\cdot}183 \pm 0{\cdot}006$, with quantities (in picograms) of 3–6 (Re), 21 (Pd), 3 (Pt), 51–59 (Ru), 12–15 (Ir) and 0·3–0·5 (Os). These blanks resulted in negligible corrections to samples (<5%) except for blank additions to AK1017L for Ir (19%) and Ru (26%), and to AK1023-8 for Re (10%) (Supplementary Data Table S1). A peridotite standard, MUH-1, was run with samples three times during the analytical campaign, and concentrations and isotopic compositions for this standard reference material are within uncertainty of a larger suite of measurements made using both Carius tube and high-pressure asher digestion methods (Meisel & Horan, 2016). Data for blue, black and red splits reported in Table 2 refer to the different aliquots of MUH-1 provided by T. Meisel.

RESULTS

Samples and sample locations

A total of 19 xenoliths and three volcanic rocks from Aitutaki were examined in this study and were obtained from two locations on the main island of Aitutaki (red locations, Fig. 1). Xenoliths and lavas AK1005 to AK1017 were obtained at outcrop at 18°49′56"S, 159°46′26"W and xenoliths AK1023 to AK1029 were obtained from a small quarry at 18°50′15"S, 159°46′9"W. Lava AK1020 is from the islet of Rapota (18°55′46"S, 159°45′26"W) and AK1025 is from a roadside outcrop at 18°50′22"S, 159°47′05"W.

Petrography and mineral chemistry

The majority of xenolith samples are spinel lherzolites ($n = 12$; ~80% modal olivine, ~15% modal orthopyroxene, ~5% modal clinopyroxene), with single examples of spinel-bearing dunite, harzburgite and olivine websterite, and four pyroxenites. Two of the lherzolites (AK1023A and B) are characterized by having zoned spinel cores (from Fe-rich cores to Fe-poor exteriors) surrounded by orthopyroxene reaction rims with FeNi metal blebs enclosed within (Fig. 2a and b; Supplementary Data Fig. S1). Lherzolite xenoliths appeared fresh within the host volcanic rocks, but the reaction rims occurring in AK1023A and B give the appearance of patchy alteration. Grain sizes for silicate phases in the xenoliths range from 0·5 to 5 mm in maximum dimension, in contrast to the volcanic rocks, which have an aphanitic matrix. The peridotites exhibit a range of textures from xenomorphic granular to poikilitic (Fig. 2a–e; Fodor *et al.*, 1982), and in some cases have a strong lineation of silicate grains (e.g. AK 1023A), or kink-banded olivine (AK1021). Textures are also consistent with melt–rock reaction processes in some samples. For example, poikilitic textures are observed around both orthopyroxene and clinopyroxene in AK1028, cooled basaltic melt pockets and vesicles occur within AK1026, and in AK1017 there is brown fibrous vitrophyre surrounding clinopyroxene. Melt–rock reaction is also evident where xenoliths are enclosed within lavas, with mineral replacement and smaller grain sizes in these regions (e.g. AK1006).

Aitutaki volcanic rocks range in composition from nephelinites to alkali basalts, with nephelinites containing xenoliths as well as large megacrysts (5–10 cm in maximum length) of pyroxene and ilmenite (Fig. 2f). Visually, the volcanic rock and xenolith samples are similar to those described in the only previous studies of Aitutaki xenoliths, by Wood (1978) and Fodor *et al.* (1982). Those researchers noted that the nephelinite hosting the xenoliths is olivine-microporphyritic, with a microcrystalline groundmass of olivine, clinopyroxene, magnetite–ilmenite oxides, and interstitial nepheline, whereas the lherzolite xenoliths vary in proportions of olivine, clinopyroxene and orthopyroxene, with pervasive evidence of reaction with melt; our observations are consistent with this assessment, although we also note the presence of large (>0·5 mm) interstitial sulfides in some of the spinel lherzolites, and abundant sulfides in the pyroxenites.

Olivine compositions for Aitutaki xenoliths range from Fo_{88} to $Fo_{90{\cdot}9}$, with low CaO (<0·1 wt %), and NiO that correlates with increasing Fo content. Orthopyroxene grains have Mg/(Mg + Fe) in equilibrium with the olivine grains (88·8–90·5) with average compositions $En_{89}Fs_{10}Wo_1$. Compared with residual abyssal peridotites, olivine grains from Aitutaki xenoliths have generally lower forsterite contents (Fig. 3), and no xenoliths were measured extending to the high Fo contents ($Fo_{90–92}$) reported by Fodor *et al.* (1982).

Whole-rock major and trace element abundances

Major and trace element data for Aitutaki samples are presented in Table 1. Xenoliths can be distinguished by their Al contents, with low-Al samples encompassing the peridotite xenoliths (<5 wt % Al_2O_3); these samples have similar major element compositions to residual abyssal peridotites (Fig. 4). The pyroxenites (including the olivine websterite sample) have higher Al contents and trend to more incompatible element-rich compositions with decreasing MgO content. The lherzolites span a range of MgO (35·3–41·2 wt %) and Al_2O_3 (2·08–4·53 wt %), with the harzburgite having 41·8 wt % MgO and 1·52 wt % Al_2O_3, and the dunite having 46·7 wt % MgO and 0·26 wt % Al_2O_3. Concentrations of MgO (14·6–28·6 wt %) are much lower and Al_2O_3 (5·75–8·91 wt %) higher in the pyroxenite xenoliths. Loss on ignition for the xenoliths ranges from 0·3 to 4 wt % and corresponds to visual evidence for limited alteration to samples. There is only weak correlation between loss on ignition (LOI) and Sr, Pb, or U and other fluid-mobile elements for the xenoliths, indicating limited post-eruptive alteration (Supplementary Data).

We analyzed three volcanic rocks from Aitutaki; nephelinite that hosts the xenoliths (AK1017), an ankaramite clast (AK1025) that is associated with AK1024 (measured by Jackson *et al.*, 2019), and an alkali basalt

Downloaded from https://academic.oup.com/petrology/article/60/9/1753/5613188 by UCSD-Philosophy user on 11 July 2024

Table 2: Re–Os isotope and highly siderophile element abundance data (in ppb) for Aitutaki xenoliths and lavas

Sample	Lithology	Eruption age (Ma)		Fo	±1SD	Al_2O_3 (wt %)	MgO (wt %)	Re	Pd	Pt	Ru	Ir	Os	$^{187}Re/^{188}Os$	2σ	$^{187}Os/^{188}Os$	2σ	$^{187}Os/^{188}Os_I$	T_{RD} age (Ma)
AK1008	Dunite	<1·4				0·26	46·7	0·086	6·258	5·787	7·749	3·517	1·798	0·225	0·003	0·12368	0·00009	0·12367	833
AK1027	Harzburgite	<1·4		90·8	0·1	1·52	41·8	0·080	6·355	10·30	6·402	3·220	2·048	0·184	0·003	0·12974	0·00009	0·12974	
AK1006	Lherzolite	<1·4		89·5	0·2	2·98	39·3	0·101	4·527	3·616	3·561	1·484	2·406	0·202	0·003	0·13171	0·00006	0·13171	
AK1023-6	Lherzolite	<1·4		90·6	0·1	2·35	35·3	0·146	3·231	2·700	4·075	1·847	1·222	0·575	0·009	0·12461	0·00009	0·12460	703
AK1023-3	Pyroxenite	<1·4				7·46	18·7	0·264	0·692	0·342	0·526	0·217	0·116	11·01	0·17	0·13471	0·00019	0·13445	
AK1023-B	Lherzolite	<1·4		89·4	0·3	4·43	36·6	0·065	2·351	4·123	4·152	2·136	0·779	0·399	0·006	0·12923	0·00009	0·12922	53
AK1017	Lherzolite	<1·4		90·0	0·1	3·00	40·1	0·063	3·829	3·528	4·717	2·367	2·049	0·149	0·002	0·12505	0·00009	0·12505	640
AK1023-4	Lherzolite	<1·4		90·1	0·1	2·08	39·8	0·057	3·062	8·208	6·545	3·255	4·259	0·064	0·001	0·12776	0·00010	0·12776	259
AK1023-A	Lherzolite	<1·4		89·6	0·1	4·53	35·6	0·077	2·483	4·934	5·230	2·703	0·824	0·452	0·007	0·12799	0·00011	0·12798	229
AK1023-7	Lherzolite	<1·4		90·3	0·1	2·24	38·2	0·085	4·561	5·647	7·045	3·080	2·498	0·164	0·002	0·12952	0·00007	0·12951	
AK1026	Pyroxenite	<1·4				8·31	14·6	0·052	1·660	0·238	0·196	0·039	0·049	5·13	0·08	0·13221	0·00047	0·13209	
AK1021	Lherzolite	<1·4	A split	90·5	0·2	3·23	41·2	0·570	0·798	2·647	2·402	1·189	0·845	3·25	0·05	0·11849	0·00010	0·11842	1562
AK1021	Lherzolite	<1·4	B split	90·5	0·2	3·23	41·2	0·011	0·937	3·389	2·966	1·725	0·854	0·062	0·001	0·11883	0·00006	0·11883	1505
AK1028	Websterite	<1·4	A split	88·2	0·1	8·91	28·6	0·040	2·516	4·105	5·482	2·655	1·114	0·173	0·003	0·12628	0·00007	0·12628	
AK1028	Websterite	<1·4	B split	88·2	0·1	8·91	28·6	0·056	4·829	5·546	2·349	1·455	0·681	0·394	0·006	0·14689	0·00012	0·14689	
AK1023-8	Lherzolite	<1·4		89·7	0·1	3·62	36·4	0·035	3·730	4·564	4·141	2·096	0·531	0·322	0·005	0·12963	0·00015	0·12963	
AL1023-2	Pyroxenite	<1·4				5·75	22·8	0·196	1·122	1·119	1·044	0·563	0·325	2·90	0·04	0·12811	0·00013	0·12804	
AK1017 L	Nephelinite	<1·4				11·7	11·3	0·085	2·034	0·177	0·224	0·062	0·042	9·79	0·15	0·13582	0·00023	0·13559	
AK1025 L	Basanite	~9·5				9·4	15·5	0·158	1·790	1·284	0·471	0·182	0·250	3·06	0·05	0·13673	0·00016	0·13625	
MUH-1 Blue	SRM		Blue split					0·204	11·77	7·970	8·472	3·717	5·311	0·185	0·003	0·12599	0·00008		
MUH-1 Red	SRM		Red split					0·215	9·721	6·916	9·767	3·740	4·688	0·221	0·003	0·12535	0·00008		
MUH-1 Black	SRM		Black split					0·207	10·39	7·487	7·326	3·468	3·581	0·278	0·004	0·12687	0·00009		

Downloaded from https://academic.oup.com/petrology/article/60/9/1753/5613188 by UCSD-Philosophy user on 11 July 2024

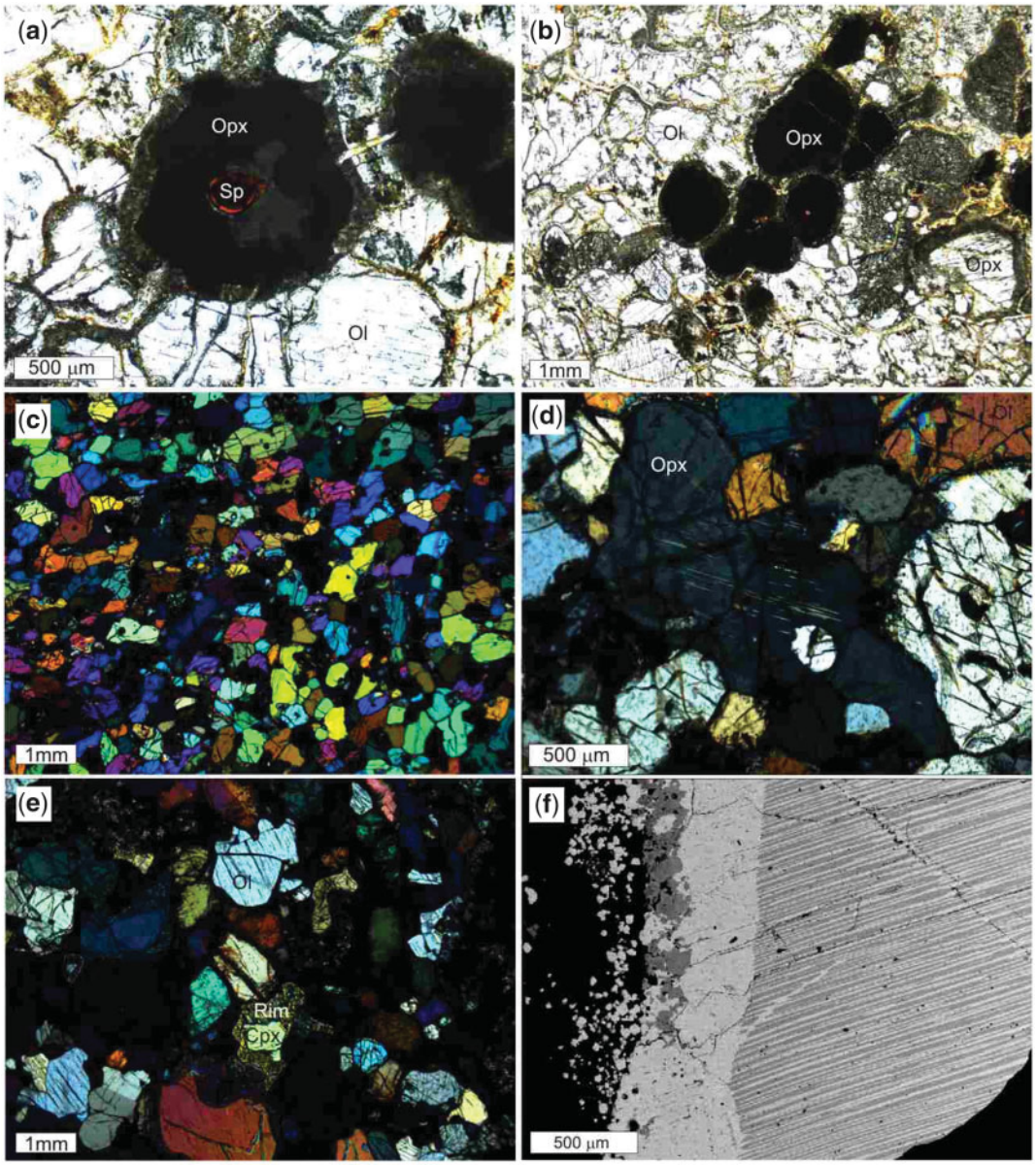

Fig. 2. (a) Lherzolite AK1023A in plane-polarized light (PPL); (b) PPL image of lherzolite AK1023B; (c) cross-polarized light (XPL) image of clinopyroxenite AK1026; (d) XPL image of pyroxenite AK1029 with an example of an orthopyroxene with exsolution lamellae; (e) XPL image of spinel lherzolite AK1028 with poikiloblastic overgrowths around clinopyroxene and olivine (labelled as Rim); (f) back-scattered electron image of comb-textured ilmenite–titanium magnetite exsolution in a megacryst from AK 1017 nephelinite. Sp, spinel; Ol, olivine; Opx, orthopyroxene; Cpx, clinopyroxene.

(AK1020). The lavas range from 11·3 to 15·5 wt % MgO with high Al_2O_3 (9·4–11·7 wt %), CaO (10·2–13·4 wt %) and TiO_2 (2–2·8 wt %), and loss on ignition from 2·3 to 4·1 wt %. Our result for the nephelinite composition is in good agreement with the Aitutaki nephelinite composition reported by Fodor *et al.* (1982).

There are generally higher concentrations of compatible elements in the lherzolite, dunite and harzburgite (peridotite) xenoliths (177–3392 ppm Cr, 1106–2416 ppm Ni, 80–133 ppm Co) compared with the lavas (202–1150 ppm Cr, 167–565 ppm Ni, 63–70 ppm Co), with the pyroxenite xenoliths lying generally intermediate to these values (643–3544 ppm Cr, 231–997 ppm Ni, 44–79 ppm Co). In primitive mantle normalized incompatible trace element plots (Fig. 5), the peridotite xenoliths show relative depletions in K, Ti, Zr, and Hf, and relative enrichments in U, Pb, and Sr, which are far less pronounced than observed in abyssal peridotites (Day *et al.*, 2017). The Aitutaki peridotites have generally higher large ion lithophile elements (LILE) and high field strength elements (HFSE), but similar rare earth element (REE) abundances compared with abyssal peridotites. Peridotites AK-1005, AK-1006, and AK-1017 also have substantially elevated Cs and Rb. In general, abundances of the incompatible trace elements are $<10\times$ and $>0{\cdot}1\times$ primitive mantle (PM) values.

Downloaded from https://academic.oup.com/petrology/article/60/9/1753/5613188 by UCSD-Philosophy user on 11 July 2024

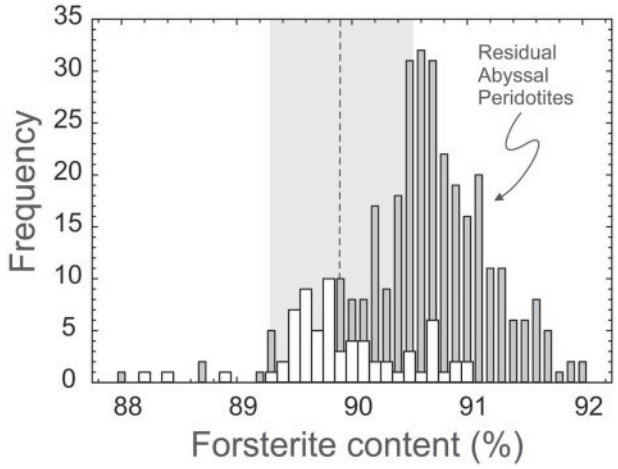

Fig. 3. Olivine forsterite histogram of Aitutaki xenoliths (open bars) vs residual abyssal peridotites. Aitutaki olivine compositions average $Fo_{89.9\pm1.2}$ (2SD; dashed line with grey error bars). Residual abyssal peridotite data are from the compilation of Warren (2016).

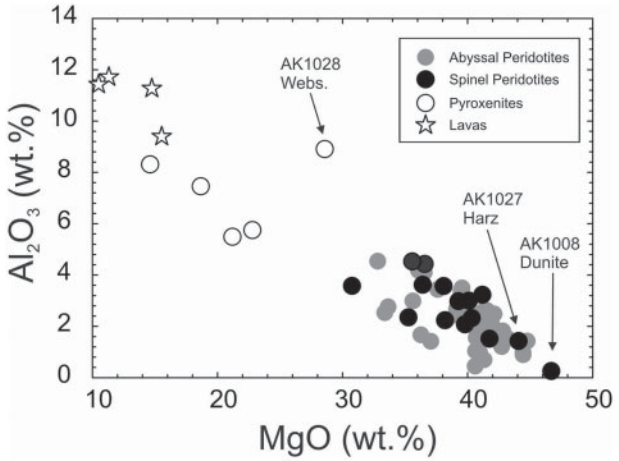

Fig. 4. Bulk-rock MgO vs Al_2O_3 for Aitutaki xenoliths and lavas measured in this study and from Fodor *et al.* (1982) vs abyssal peridotite compositions from Day *et al.* (2017).

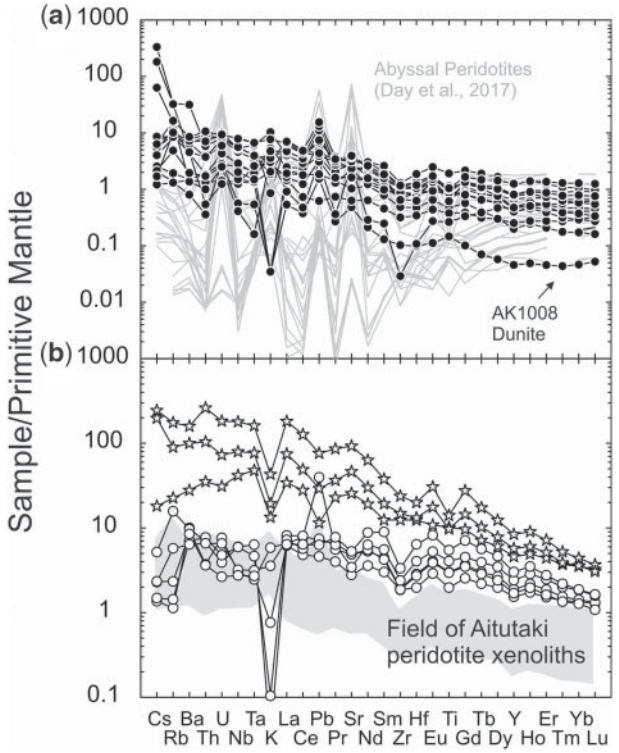

Fig. 5. Primitive mantle normalized plot of (a) Aitutaki spinel lherzolite, harzburgite and dunite xenoliths, and (b) pyroxenite xenoliths (open circles) and lavas (open stars). Field of Aitutaki xenoliths in (b) shows samples in panel (a). Abyssal peridotite compositions from Day *et al.* (2017) are shown in (a). Primitive mantle normalization from McDonough & Sun (1995).

Pyroxenite xenoliths show slight negative anomalies in Zr and Ti, and depletions in K, Rb and Cs (Fig. 5). In general, abundances of the incompatible trace elements are $<20\times$ and $>0{\cdot}1\times$ PM values and are typical for Aitutaki lavas and similar to other Pacific enriched mantle (EM) ocean island basalts (Fig. 6). Volcanic rocks show much greater enrichment in incompatible trace elements than the pyroxenite xenoliths, but have similar primitive mantle-normalized patterns. Comparison of the lavas analyzed in this study with those from Jackson *et al.* (2019) illustrates that AK1025 is depleted in the LILE, as also seen in AK1024 that is dated at ~9·5 Ma. Samples AK1017L and AK1020, on the other hand, have similar compositions to Aitutaki younger volcanic rocks.

Highly siderophile element (HSE) abundances and osmium isotope systematics

Whereas all samples examined in this study were measured for major and trace element abundances, owing to limited available masses AK1029, AK1020, AK1023-1, AK1023-5, AK1006, and AK1005 were not measured for $^{187}Os/^{188}Os$ and HSE abundances. Furthermore, the restriction in sample mass (sometimes <5 g) meant that samples were generally measured once, except for samples AK1021 and AK1028, which were both measured twice, using different fragments of the xenoliths that were crushed and powdered separately to determine the possibility of centimeter-scale heterogeneities within each sample, and are referred to as AK1021-A, AK1021-B, AK1028-A, and AK1028-B.

The HSE (Os, Ir, Ru, Pt, Pd, Re) concentrations of one dunite, one harzburgite, nine lherzolites, three pyroxenites, one olivine websterite, and two volcanic rocks (an ankaramite and nephelinite), are reported in Table 2. In general, the peridotite xenoliths have broadly flat to humped PM-normalized HSE patterns ranging between ~0·1× and 1× PM values (Fig. 7a). Samples AK1021-A and AK1021-B, taken from a single xenolith, represent the most enriched and depleted samples for Re (0·011–0·57 ppb), and are also most depleted in Pd (0·8–0·94 ppb) compared with the range of other lherzolite samples (2·35–4·56 ppb). These samples did not look obviously different prior to preparation, and so we

Downloaded from https://academic.oup.com/petrology/article/60/9/1753/5613188 by UCSD-Philosophy user on 11 July 2024

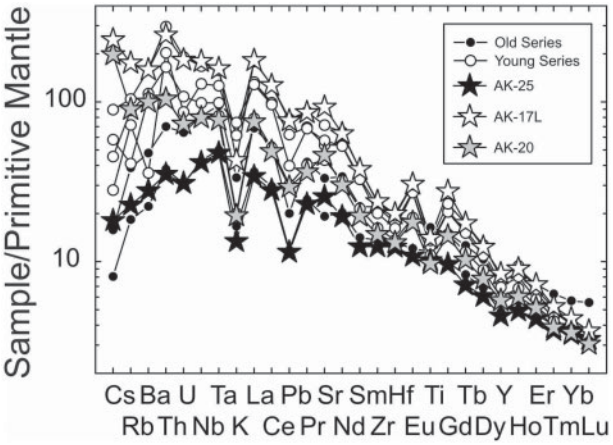

Fig. 6. Primitive mantle normalized plot of Aitutaki lava samples measured in this study (AK1017L, AK1020, AK1025) vs young and old series volcanic rocks from Jackson *et al.* (2019). Normalization is the same as for Fig. 5.

attribute these differences to chemical variations in the samples. The olivine websterite has broadly similar HSE abundances to the lherzolites, whereas the pyroxenite xenoliths have steep HSE patterns with pronounced relative depletions in Ru, Ir and Os relative to Pt and Pd, and, in this respect, are similar to the lavas (Fig. 7b). The pyroxenite xenoliths exhibit variable concentrations in Os (0·049–1·11 ppb), Ir (0·039–2·66 ppb), Ru (0·196–5·48 ppb), Pt (0·238–5·55 ppb), Pd (0·692–4·83 ppb), and Re (0·040–0·264 ppb), with the websterite sample having Os, Ir and Ru contents similar to some of the peridotites. Volcanic rocks have similar PM-normalized patterns, with the exception of Pt and Ir, both of which are more depleted in the nephelinite sample. The peridotite xenoliths have PM-normalized Ru/Ir (dunite + harzburgite = 0·96 ± 0·05; lherzolites = 0·93 ± 0·09; 1SD) similar to abyssal peridotites (Ru/Ir = 1·25 ± 1·15; Day *et al.*, 2017), but Os/Ir ratios that are generally lower [dunite + harzburgite = 0·53 ± 0·06; lherzolites = 0·68 ± 0·39 versus 0·88 ± 0·24 in abyssal peridotites (Day *et al.*, 2017)].

Age corrections for ^{187}Os ingrowth owing to Re decay since eruption are trivial for the lava and xenolith samples (Table 2). The spinel-bearing peridotites have $^{187}Os/^{188}Os$ ranging from 0·1185 to 0·1317 (average and 2SD = 0·1264 ± 0·0082). These samples have generally low $^{187}Re/^{188}Os$ values (<0·6), with the exception of AK1021-A, which has a notably higher value compared with AK1021-B, indicating significant heterogeneity at the centimeter scale for Re in this xenolith (Fig. 8). The pyroxenite xenoliths show much more variable ratios for both $^{187}Os/^{188}Os$ (0·1263–0·1469) and $^{187}Re/^{188}Os$ (0·173–11·0) than the peridotite xenoliths. The volcanic rocks are more radiogenic than the peridotites, with $^{187}Os/^{188}Os$ corrected for time of eruption of 0·1356–0·1363.

Standard reference material, harzburgite MUH-1 (aliquots red, blue and black, from T. Meisel, University of Leoben, Austria) was also analyzed in this study and

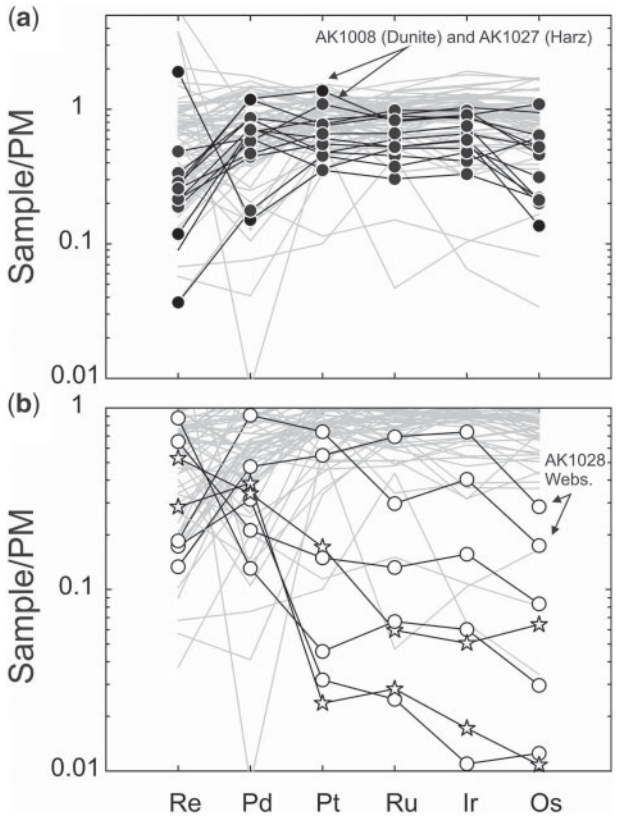

Fig. 7. Primitive mantle normalized highly siderophile element patterns for (a) Aitutaki lherzolite, harzburgite and dunite xenoliths, and (b) pyroxenite xenoliths and lavas, vs abyssal peridotite compositions from Day *et al.* (2017). Data are plotted with the most incompatible elements on the left. Symbols are the same as for Fig. 5.

values are reported in Table 2. Average abundances (in ppb, with 2SD) are Re = 0·21 ± 0·02 (3% RSD), Pd = 10·6 ± 2·0 (10% RSD), Pt = 7·5 ± 1·1 (7% RSD), Ru = 8·5 ± 2·4 (14% RSD), Ir = 3·64 ± 0·30 (4% RSD), and Os = 4·53 ± 1·76 (19% RSD), with $^{187}Re/^{188}Os$ = 0·23 ± 0·05 and $^{187}Os/^{188}Os$ = 0·1261 ± 0·0015 (0·6% RSD). The MUH-1 standard is considered representative of refractory peridotites, with the high RSDs for some elements reflecting nugget heterogeneities from inhomogeneous distribution of Os–Ru alloys and sulfides (e.g. Meisel & Horan, 2016).

DISCUSSION

Rejuvenated volcanic rocks formed by low-degree melting of an OIB source

Before considering the origin and implications of Aitutaki xenolith geochemical compositions, it is important to understand the origin of the volcanic rocks that exhumed them. Aitutaki is part of the Cook Islands and the westernmost of the volcanoes with exposed volcanic rocks of the Cook–Austral hotspot track (Fig. 1; e.g. Clouard & Gerbault, 2008). The hotspot responsible for Aitutaki was originally considered to be related to the Macdonald seamount (Morgan, 1972), but older

Downloaded from https://academic.oup.com/petrology/article/60/9/1753/5613188 by UCSD-Philosophy user on 11 July 2024

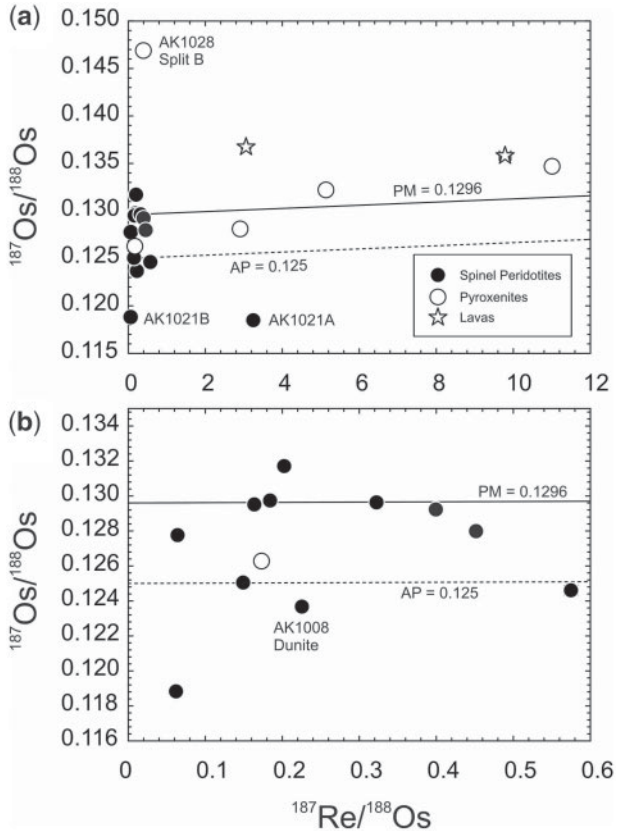

Fig. 8. $^{187}Re/^{188}Os$–$^{187}Os/^{188}Os$ diagrams for (a) Aitutaki xenoliths and lavas and (b) only Aitutaki peridotites. The figure shows 100 Ma reference isochrons assuming primitive mantle $^{187}Os/^{188}Os$ (PM = 0·1296) and abyssal peridotite (AP = 0·125) isotope evolution.

series volcanism on the island is now considered to be part of the Arago seamount trend, with the younger volcanism associated with Rarotonga (Chauvel *et al.*, 1997). Volcanism responsible for the generation of Aitutaki occurred on relatively old Pacific Ocean lithosphere, estimated at ~90 Ma (Calmant *et al.*, 1990). A minor volume of Aitutaki's volcanic rocks are exposed subaerially, and are composed of nephelinite, basanite and alkali basalt (Wood, 1967, 1978). The majority of exposed volcanic rocks appear to have been erupted broadly contemporaneously, based on K/Ar and $^{40}Ar/^{39}Ar$ age dating. The average age of nephelinite hosting the xenoliths is between 0·72 ± 0·06 Ma (Dalrymple *et al.*, 1975) and 1·13 ± 0·26 Ma (Turner & Jarrard, 1982) based on K/Ar dating, with nephelinites from Rapota and Moturakau being older based on $^{40}Ar/^{39}Ar$ ages (1·72–1·94 Ma; Rose & Koppers, 2019). These ages are similar to those of olivine basalts measured from the tuff ring of the main island (1·38–1·43 Ma; Rose & Koppers, 2019) and indicative of a 'cap' of young volcanic rocks on Aitutaki volcano, termed the 'young volcanic series', including samples AK1017 and AK1020 from this study. An 'old volcanic series' has also been recognized based on K/Ar and $^{40}Ar/^{39}Ar$ ages for a single alkali basalt clast (AIT-36) in the tuff ring dated at 9·53 ± 0·08 Ma (Turner & Jarrard, 1982; Rose & Koppers, 2019). The 'old volcanic series' have lower LILE abundances than 'young volcanic series' rocks (Jackson *et al.*, 2019), consistent with the composition measured for AK1025, and we therefore assign this sample to the 'old volcanic series' grouping (Fig. 6). All of the older volcanic series lavas recognized thus far are clasts.

To estimate the degree and depth of partial melting, an incremental batch partial melt model was computed (Fig. 9). We chose a primitive mantle starting composition, reflecting the trace element enriched nature of the Aitutaki lavas. The calculated partial melting curves indicate low-degree (2%) partial melting exclusively in the garnet stability field for the nephelinite. The alkali basalts are from 3–5% partial melting of enriched mantle sources via melting in both the spinel and garnet stability fields. Comparison of incompatible trace element (ITE) abundances for the three Aitutaki volcanic rocks shows the progressive increase in ITE abundances from the alkali basalts to the nephelinite (Fig. 6). It has previously been shown that Aitutaki volcanic rocks have EM1 or EM2 ocean island basalt (OIB)-type signatures ($^{87}Sr/^{86}Sr$ = 0·70440–0·70506; $^{143}Nd/^{144}Nd$ = 0·512715–0·512789; Nakamura and Tatsumoto, 1988; Schiano *et al.*, 2001). Both young and old series Aitutaki volcanic rocks have steeper HSE patterns than Hawaii (Ireland *et al.*, 2009) and compare closely with Canary Island alkali basalt lavas (Day *et al.*, 2010), except for greater depletion in Re and Pt in Aitutaki. Aitutaki melts also have radiogenic $^{187}Os/^{188}Os$ signatures (0·1356–0·1363; Fig. 8), identical within uncertainties to that previously measured for an Aitutaki volcanic rock of 0·1370 (Schiano *et al.*, 2001). Collectively, the Os–Sr–Nd isotope compositions of the Aitutaki volcanic rocks are consistent with an origin from EM-type mantle sources both for 'old volcanic series' and 'young volcanic series' rocks. Low degrees of partial melting in the garnet stability field and the young age (~1·1–1·2 Ma) of the nephelinite that erupted the Aitutaki xenolith suite are consistent with either 'Richter rolls' (Turner & Jarrard, 1982) or rejuvenated volcanism induced by lithospheric flexure from loading of the local plate by Rarotonga subaerial lavas, which range in age from ~1·16 to 1·70 Ma (Dalrymple *et al.*, 1975; Rose & Koppers, 2019).

Melt infiltration beneath Aitutaki

The Aitutaki pyroxenite xenoliths are generally finer grained (Fig. 2) than the lherzolites, dunite and harzburgite (peridotites) and have Al_2O_3 and MgO contents and incompatible trace element compositions intermediate between peridotites and lavas (e.g. Figs 4 and 5). The pyroxenite xenoliths span a range of compositions from AK1028, which has total HSE abundances (Σ_{HSE} = 15–16 ppb) similar to those of the peridotites (Σ_{HSE} = 8–28 ppb), to the pyroxenite AK1026, which has incompatible trace element and HSE abundances and $^{187}Os/^{188}Os$ approaching those of the host volcanic

Downloaded from https://academic.oup.com/petrology/article/60/9/1753/5613188 by UCSD-Philosophy user on 11 July 2024

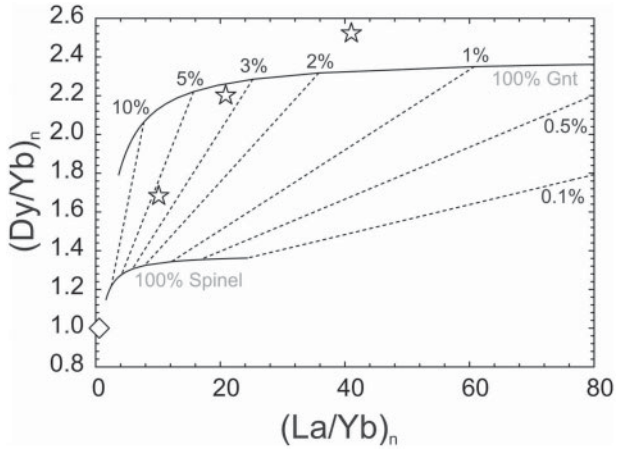

Fig. 9. Estimates of partial melting for Aitutaki lavas (stars) vs a typical normal mid-ocean ridge basalt (N-MORB) composition (diamond). The model assumes a primitive mantle source (Sun & McDonough 1989) with garnet peridotite starting modal proportions of olivine, orthopyroxene, clinopyroxene, and garnet of 0·598/0·211/0·076/0·115 and a spinel peridotite with olivine, orthopyroxene, clinopyroxene, and spinel of 0·578/0·21/0·119/0·033, with melting and partitioning phases equal to those given by McKenzie & O'Nions (1991).

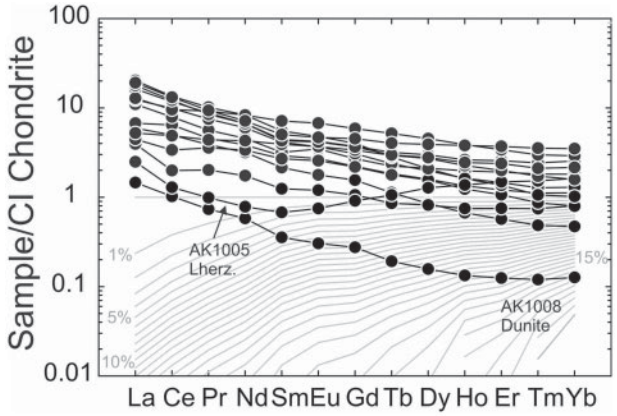

Fig. 10. CI-chondrite normalized plot of Aitutaki lherzolite, harzburgite and dunite xenoliths. Grey lines indicate 1% melt increments for a non-modal fractional melting model, where increasing melt depletion results in lower absolute abundances of the REE and increasing depletion in the LREE (e.g. La) relative to the HREE (e.g. Yb). To estimate melt depletion, we use a non-modal fractional melting model for whole-rock abyssal peridotites that assumes an initial starting composition of depleted MORB mantle (Workman & Hart, 2005), and uses partition coefficients from Suhr *et al.* (1998) for spinel and Sun & Liang (2014) for olivine and pyroxene, and melt reactions discussed by Warren (2016). The model leads to general levels of melt depletion similar to those calculated using the spinel compositions. Model parameters and normalization are from Day *et al.* (2017).

rocks. These variations probably reflect crystallization of melts to form pure cumulate pyroxenite (e.g. AK1026), to variable crystallization of melts within existing peridotite (Fig. 7b). This form of melt infiltration can explain the wide range in relative and absolute abundances of the HSE and $^{187}Os/^{188}Os$ in the pyroxenites, with the addition of these elements within metasomatic base metal sulfide (BMS) precipitated from silicate melts. Previous workers have shown that minor quantities (<0·05 wt %) of metasomatic BMS precipitated or removed are typically involved with limited volumes of S-saturated melts during melt infiltration processes (e.g. Lorand & Luguet, 2016). These results imply that the melts infiltrating the xenoliths and directly crystallizing pyroxenite were similar in composition to those responsible for generating Aitutaki volcanism.

From the Aitutaki xenolith suite, it is also evident that melt–rock reaction with peridotite was probably operating from the scale of the lithosphere to the centimeter scale, based on both trace element and HSE results. Our analysis of two separate splits of AK1028 shows distinct $^{187}Os/^{188}Os$ (0·1263 versus 0·1469) and HSE abundance variations of >35%, exceeding the variation expected even for refractory peridotites such as the standard reference material, MUH-1. The Re–Os isotope systematics of AK1028 is not consistent with recent Re addition to samples, instead indicating that unsupported $^{187}Os/^{188}Os$ occurs in AK1028-B either from precipitation of BMS from radiogenic melt or from long-term ingrowth of ^{187}Os after addition of Re in the mantle.

The peridotite xenoliths exhibit variable extents of melt–rock reaction, including light REE (LREE) inflections similar to the lavas (Fig. 10), relatively high incompatible trace element abundances, and in one case (AK1021-A) elevated Re contents. We find that melt depletion for the lherzolites and harzburgites estimated from the heavy REE (HREE) are similar to those of abyssal peridotites (Fig. 10), with the single Aitutaki dunite xenolith (AK1008) preserving evidence for extreme melt depletion (~20%), suggesting that it may represent a fragment of a highly depleted melt-channel. The peridotite xenoliths generally cluster to low Al_2O_3 and high MgO contents, like abyssal peridotites (Fig. 4). Basaltic melts typically have more radiogenic $^{187}Os/^{188}Os$ but substantially lower Os contents than peridotites, meaning that only high degrees of melt–rock reaction will lead to modification of peridotite HSE compositions. For example, the Aitutaki lavas compositions are similar in composition to average alkali basalts (Os ~0·067 ppb; $^{187}Os/^{188}Os$ ~0·146; Day, 2013) and average mid-ocean ridge basalts (Os ~0·010 ppb; $^{187}Os/^{188}Os$ ~0·133; Gannoun *et al.*, 2016), which have limited (<1%) effects on $^{187}Os/^{188}Os$ in the peridotites, until high melt–rock ratios (>10). This explains why the patterns for the olivine websterite is more similar to the peridotite xenoliths than to the lavas or pyroxenite xenoliths, suggesting a threshold for melt–rock reaction to strongly affect the HSE, and consequently for the precipitation of metasomatic BMS.

There are positive relationships between Pd/Pt, Ru/Ir, Pd/Ir and $^{187}Os/^{188}Os$ for Aitutaki peridotites, implying a limited role for precipitation and removal of BMS in the samples (Fig. 11). A simple mixing model between the most melt-depleted spinel lherzolite and lava and pyroxenite indicates that significant addition of melt would be required to explain these relationships. Orders of

Downloaded from https://academic.oup.com/petrology/article/60/9/1753/5613188 by UCSD-Philosophy user on 11 July 2024

magnitude less melt infiltration is required from preferential incorporation of HSE from BMS without incorporation of silicate melt. It has previously been proposed that melt refertilization, possibly prior to incorporation of the peridotites into the lithosphere, may play a role in generating not only the high Pd/Ir found in some peridotite suites, but also elevated Ru/Ir (e.g. Day *et al.*, 2017). Melt–rock reaction is highly variable in the Aitutaki xenolith suite, from complete crystallization of melts (some pyroxenites) to extensive reaction (pyroxenites), to minor or cryptic metasomatism by BMS (peridotites).

Low Os/Ir in Aitutaki samples

A feature of some of the Aitutaki peridotites is their low Os/Ir ratios, which can be up to 40% lower than in abyssal peridotites. In contrast, the peridotites have Ru/Ir ratios that are within the range of abyssal peridotites. In addition to low Os/Ir in the peridotites, the pyroxenite xenoliths also preserve this feature. The low Os/Ir does not appear to have been caused by sample preparation or analytical issues, with the MUH-1 peridotite run with samples yielding typical Os/Ir and Ru/Ir ratios. Instead, it is possible that Os has been lost by complex weathering or oxidative weathering processes at or near the surface, as proposed previously (van der Meer *et al.*, 2017). Alternatively, Os loss may also have occurred during infiltration by oxidizing melts. The generally pronounced depletions in Os relative to Ir in the pyroxenites (Fig. 7) hint at Os loss during melt infiltration processes or during eruption. In contrast, there is no evidence for either ancient Os loss or Os loss by weathering processes, where no relationship is observed with Os content and LOI (see Supplementary Data).

Heterogeneity within the lithosphere of Aitutaki

Aitutaki Island sits atop 80–90 km thick lithosphere (e.g. Sclater & Francheteau, 1970) based on the estimated lithospheric age (Calmant *et al.*, 1990), consistent with independent calculations for Pacific plate thickness (Ritzwoller *et al.*, 2004). We suggest that the peridotite xenoliths originate from this column of melt-depleted oceanic lithosphere. In contrast, the volcanic rocks come from a distinct and enriched mantle source. Our results imply that melts originated at a depth greater than or equal to 80–90 km in the asthenosphere, or from the asthenosphere–lithosphere boundary, based on plate thickness estimates, and entrained the xenoliths during ascent to the surface.

It has been recognized that mantle heterogeneity exists in Earth on scales ranging from thousands of kilometers to meters (e.g. Hart 1984; Hart *et al.*, 1992; Hofmann, 1997; O'Driscoll *et al.*, 2018). Harzburgites are notoriously more heterogeneous than lherzolites for refractory trace elements, such as the HSE (e.g. Luguet & Reisberg, 2016), owing to the presence of micro-inclusions of HSE-rich sulfides and alloys formed during partial melting and melt–rock reaction. The

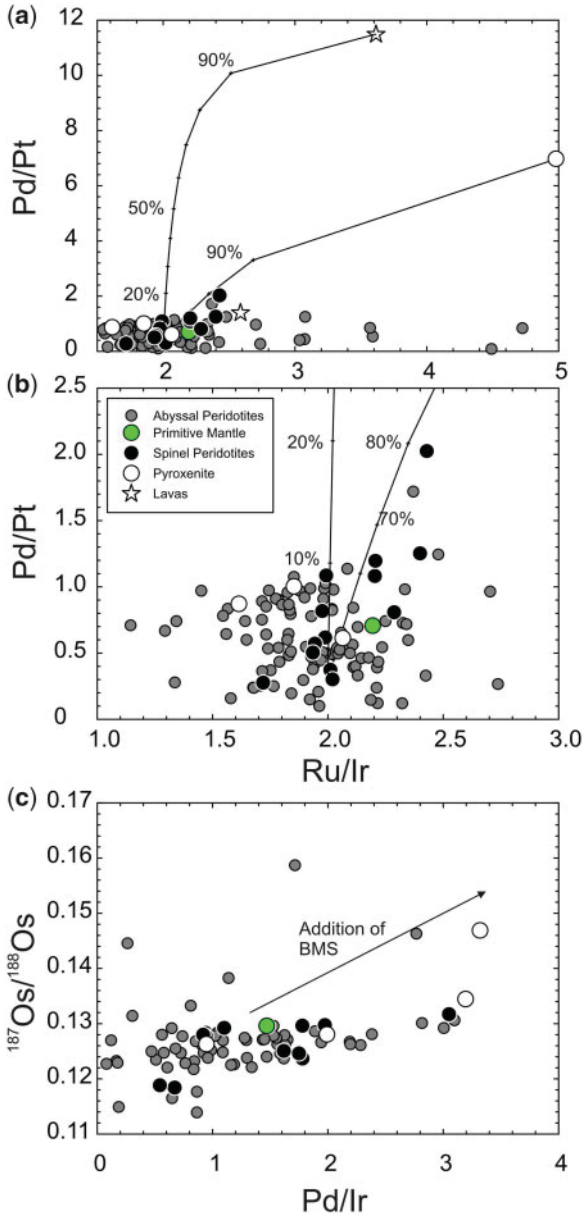

Fig. 11. Palladium/Pt vs Ru/Ir (a, b) and Pd/Ir vs $^{187}Os/^{188}Os$ (c) compositions for Aitutaki xenoliths and lavas vs abyssal peridotites and the primitive mantle composition from Day *et al.* (2017). Model shows mixing between AK1021-A lherzolite composition and a lava (AK1017L) and a pyroxenite (AK1026) in terms of 10% increments of melt addition to explain the HSE ratios. Orders of magnitude lower melt addition is required assuming that the HSE are hosted in metasomatic BMS.

harzburgite standard reference material MUH-1 provides an example of the heterogeneity that might be expected from the 'nugget effect' within individual sample powders, implying variations of 20% or more with respect to absolute concentrations of the HSE. Analysis of two separate fractions of spinel lherzolite AK1021 show variations in excess of 100% for Re, and the abundance variations of the HSE for the whole Aitutaki spinel lherzolite data are >60% for Re and Os, and >35% for Pd, Pt, Ru and Ir. Sample AK1021-A has significantly higher $^{187}Re/^{188}Os$ than AK1021-B, but both are similar

Downloaded from https://academic.oup.com/petrology/article/60/9/1753/5613188 by UCSD-Philosophy user on 11 July 2024

with respect to $^{187}Os/^{188}Os$, reflecting late Re addition via melt refertilization to AK1021-A. These results suggest that 'nugget effects' from inhomogeneous distribution of the HSE in different sulfide and other HSE-bearing minerals within the samples reflect true localized heterogeneity in the oceanic mantle lithosphere beneath Aitutaki, caused by either melt refertilization (e.g. Re in AK1021) or melt depletion.

The role of melt depletion acting on mantle heterogeneity is well expressed in both Pd/Ir (Fig. 11) and Al_2O_3 versus $^{187}Os/^{188}Os$ space (Fig. 12). Because Al_2O_3 preferentially contributes to the melt during partial melting, melt depletion leads to progressive depletion of this compound, whereas $^{187}Os/^{188}Os$ tracks the time-integrated variation in the Re/Os ratio; Re and Al_2O_3 are considered to behave broadly similarly during partial melting (e.g. Luguet & Reisberg, 2016) such that recent melting would lead to only a change in Al_2O_3 content in Fig. 12, but ancient melt depletion would retard ingrowth of ^{187}Os. This effect is evident in abyssal peridotite data, where there is a broad positive relationship between Al_2O_3 and $^{187}Os/^{188}Os$, consistent with oceanic peridotites representing melt residues that have experienced melt depletion over time (e.g. Harvey *et al.*, 2006; Lassiter *et al.*, 2014; Day *et al.*, 2017). A similar relationship is observed for some Aitutaki spinel peridotite xenoliths, with some peridotites being significantly depleted in both Al_2O_3 and $^{187}Os/^{188}Os$. However, there is a spread in $^{187}Os/^{188}Os$ of between 2 and 4 wt % Al_2O_3 in Aitutaki xenoliths, suggesting that melt depletion responsible for these variations is both ancient and more modern, when the peridotites experienced melting at the Pacific spreading ridge. These observations suggest significant isotopic and elemental heterogeneity in the oceanic mantle lithosphere beneath Aitutaki, generated by both ancient and modern melt depletion in the peridotites, and by extensive melt–rock reaction and crystallization of cumulates for the pyroxenites and affiliated rocks.

Thickened lithosphere beneath the Cook Islands?

Aitutaki lherzolites represent oceanic lithosphere and generally compare with abyssal peridotites, which represent oceanic mantle that has been processed through ridges (Niu, 2004). Evidence for similarities with abyssal peridotites are evident from similar major element compositions, high concentrations of compatible elements, and similar HSE patterns. However, Aitutaki spinel lherzolites show evidence for melt infiltration by enriched OIB-type melts. A key question is whether sufficient melt–rock reaction occurred to generate clinopyroxene in the lherzolites. Although some lherzolites have poikilitic textures, where orthopyroxene is replaced by olivine (Fodor *et al.*, 1982), we observe no significant overgrowths or association with clinopyroxene in any of the lherzolites as we do with the olivine websterite (AK1028; Fig. 2e). We also note that, although LREE abundances are consistent with cryptic melt infiltration

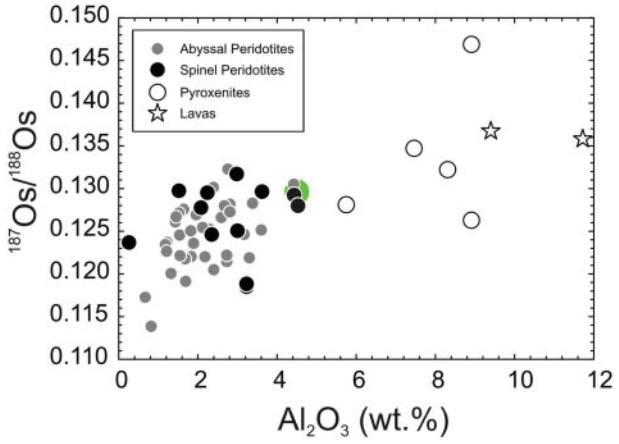

Fig. 12. Aluminum oxide vs $^{187}Os/^{188}Os$ variation diagram for Aitutaki xenoliths and lavas vs abyssal peridotite compositions from Day *et al.* (2017). Primitive mantle composition shown as a green dot from Meisel *et al.* (2001).

for most of the peridotites, the petrographic evidence for significant melt refertilization is minimal, except for the possible exception of large sulfides in some lherzolites and the pyroxenites. Finally, olivine compositions are negatively correlated with both Al_2O_3 and $^{187}Os/^{188}Os$ for the spinel lherzolites, suggesting that these xenoliths sample lithosphere that has been variably melt depleted both in time and space.

Amongst the spinel lherzolites, two samples (AK1023A and B) are notable in having elevated incompatible trace element abundances (Table 1; Fig. 5), and Al_2O_3 and $^{187}Os/^{188}Os$ overlapping the primitive mantle composition (Fig. 12). These samples have unusual associations of pink spinel (visibly pink in thin-section) completely enclosed by pyroxene with a bulk composition approaching that of orthopyroxene (see Supplementary Data tables) and having an amorphous or grainy texture at the micron scale (Supplementary Data Figs S1 and S2). The texture of these associations presumably accounts for the opaque nature of the pyroxenes in plane-polarized light (Fig. 2a and b). The spinel grains are zoned and can have complex reaction rims with the surrounding pyroxene. Remarkably, the surrounding pyroxene has FeNi metal grains (~80%Fe:20%Ni) embedded within it (Supplementary Data Figs S1 and S2, Table S3). These features are somewhat similar to kelyphite or symplectites found in some mantle peridotite xenoliths that have previously been attributed to breakdown of garnet (e.g. Smith, 1977; Spacek *et al.*, 2013; Scott *et al.*, 2014). Several different reactions are possible, depending on composition:

$$\mathrm{Grt} + \mathrm{Ol} \rightarrow \mathrm{Opx} + \mathrm{Cpx} + \mathrm{Sp}$$

or, in silica-saturated systems (e.g. Obata, 2011),

$$\mathrm{Grt} + \mathrm{Qtz} \rightarrow \mathrm{Opx} + \mathrm{An}.$$

In the case of the orthopyroxene–spinel associations in AK1023A and B, the idealized reaction would be, in the absence of Ca (Macgregor, 1974),

Downloaded from https://academic.oup.com/petrology/article/60/9/1753/5613188 by UCSD-Philosophy user on 11 July 2024

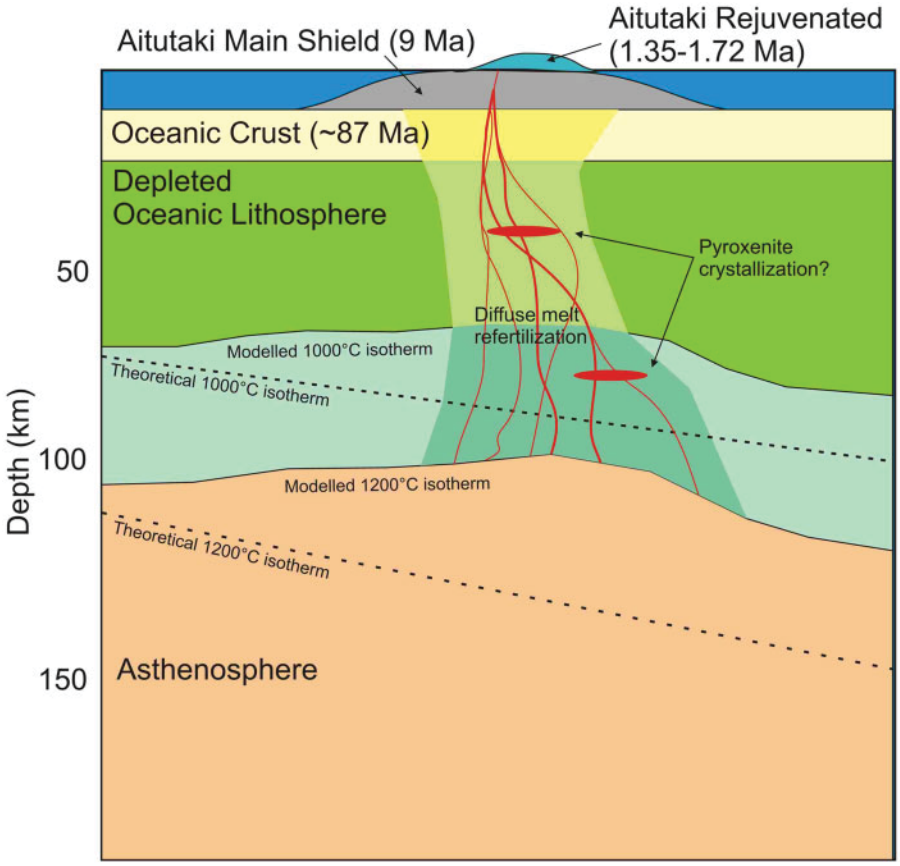

Fig. 13. Summary diagram of the formation of Aitutaki on ~90 Ma Pacific oceanic lithosphere, showing the relationship of melt infiltration (red lines are schematic melt channels) and fertilization in the lithosphere and crust beneath Aitutaki and locations of theoretical and modelled isotherms. Garnet stability is generally consistent with the modelled 1000°C isotherm. Pacific upper mantle structure from Ritzwoller *et al.* (2004).

$$\mathrm{Grt} + \mathrm{Ol} \rightarrow \mathrm{Opx} + \mathrm{Sp}.$$

Whatever the cause of the pyroxene–spinel associations in AK1023A and B, the presence of (1) FeNi metal in association with these phases and (2) the high content of Fe (Mg# ~52, Cr# ~32; Supplementary Data Table S3) in the pink spinels that are distinct from typical mantle peridotite spinel compositions (correlated from Mg# ~80, Cr# = 10 to Mg# ~40, Cr# ~55; e.g. Zhou *et al.*, 1996) makes them unusual.

The AK1023A and B lherzolites are consistent with sampling of relatively fertile—but non-pristine—mantle peridotite, possibly beginning in the garnet stability field. Fodor *et al.* (1982) reported orthopyroxene–clinopyroxene thermometry consistent with two temperatures of equilibration from 774–834°C to 1040–1140°C. Calculations of orthopyroxene compositions using the modern work of Nimis & Grütter (2010) show that the Fodor *et al.* (1982) samples, as well as AK1021 and AK1028 from our own study, fall within the previously reported temperature groupings. Fodor *et al.* (1982) suggested, based on petrography and mineral chemistry, that the Aitutaki spinel lherzolites resulted from diapiric upwelling and inversion of garnet lherzolite. The associations of spinel and orthopyroxene in AK1023A and B are permissive of this hypothesis and suggest origination from at least 70 km depth (1150°C). The observations are consistent with formation of Aitutaki Island on oceanic lithosphere where melts have sampled mantle in the garnet stability field (>70 km) as well as variably depleted oceanic lithosphere. A thickened lithosphere has been suggested for the region surrounding the Cook Islands before, based on a hotspot-volcano related volcanic 'gap' between the Cook Islands and Samoa (Sleep, 2002). This may be consistent with thickened lithosphere at a hot ridge in response to emplacement of various volcanic plateaux. Peridotite xenoliths from the Ontong Java Plateau demonstrate thickened lithosphere (<120 km), with a fertile upper region of lithosphere (<85 km), and refractory harzburgites with ancient depletion ages (0·9–1·7 Ga) from greater depths (Ishikawa *et al.*, 2011). Although the existing dataset for oceanic island peridotites is currently unable to resolve differences in composition with lithospheric depth, the Aitutaki xenoliths are consistent with originating from ~90 km thick lithosphere where magmatism led to generation of rocks formed by melt–rock reaction and melt crystallization (pyroxenites) and sampling of the entire oceanic mantle lithosphere (Fig. 13).

Downloaded from https://academic.oup.com/petrology/article/60/9/1753/5613188 by UCSD-Philosophy user on 11 July 2024

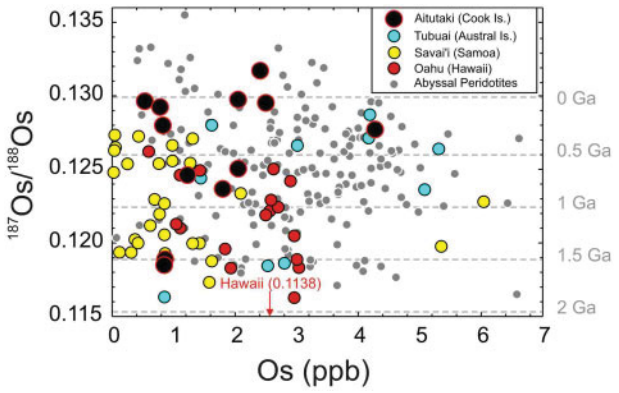

Fig. 14. Relationship between $^{187}Os/^{188}Os$ and Os concentrations for Aitutaki xenoliths compared with peridotite xenoliths from Savai'i (Samoa) and Tubuai from Jackson *et al.* (2016), Oa'hu (Hawaii) from Bizimis *et al.* (2007), and abyssal peridotites (from Day *et al.*, 2017). Depletion ages for a primitive mantle composition are shown on the right-hand side of the plot. These islands formed on ~75 Ma (Tubuai) to >100 Ma (Samoa) lithosphere, but all possess lithospheric mantle peridotite xenoliths with Mesoproteroic or older depletion ages.

Implications for the nature of Pacific lithosphere and oceanic island xenoliths

Depleted mantle components have been suggested based on major element compositions for Hawaii, Tahiti and other ocean island xenolith suites (e.g. Simon *et al.*, 2008), and have now been recognized from Re–Os isotope systematics for Hawaii (Bizimis *et al.*, 2007), Samoa and Tubuai (Jackson *et al.*, 2016), and the Cook Islands (this study). Xenoliths have preserved old melt depletion ages up to 1·5 Ga in Aitutaki, or ~2 Ga in O'ahu (Bizimis *et al.*, 2007), and Jackson *et al.* (2016) have reported old melt depletion ages in Savai'i up to 1·5 Ga and in Tubuai up to 1·8 Ga. The $^{187}Os/^{188}Os$ and Os contents for mantle xenolith suites from Aitutaki (Cook Islands), O'ahu (Hawaii), Savai'i (Samoa) and Tubuai (Austral Islands) span a similar range of compositions compared with global abyssal peridotites, despite melt–rock reaction occurring in these ocean island suites (Fig. 14). In particular, samples from the Pacific oceanic islands with the lowest $^{187}Os/^{188}Os$, and hence the oldest depletion ages, span similar maximum depletion ages to those observed for abyssal peridotites (e.g. Harvey *et al.*, 2006), from the Paleoproterozoic (~2 Ga) to the Mesoproterozoic (~1·5 Ga). Like Aitutaki mantle xenoliths, abyssal peridotites have also been measured with more radiogenic $^{187}Os/^{188}Os$ than primitive mantle estimates. Collectively, these observations indicate that if mantle xenoliths from Pacific Ocean islands, and abyssal peridotites from global ridges, are representative, then the gross geochemical structure of the Pacific lithosphere is similar to that of global oceanic lithosphere. The new results from Aitutaki support the concept of variably melt-depleted lithosphere formed through recent and ancient melt extraction events and several Wilson cycles, as has also been proposed for abyssal peridotites (e.g. Lassiter *et al.*, 2014; Day *et al.*, 2017) and ophiolites (O'Driscoll *et al.*, 2012, 2018).

Detailed trace element geochemistry and HSE abundances allow identification of melt refertilization as an important process in the generation of geochemical signatures in the Aitutaki xenolith suite. Extrapolation of this information to O'ahu, Savaii and Tubuai peridotite xenoliths leads to the inference that the variations in Os isotopic compositions seen throughout these samples may also reflect later melt-infiltration processes superimposed on prior melt depletion. The Pacific lithosphere appears similar to oceanic mantle preserved by abyssal peridotites (e.g. Lassiter *et al.*, 2014), but it can trend to generally older depletion ages. It is possible that Pacific mantle lithosphere and oceanic mantle lithosphere in general may represent strongly depleted mantle that was subjected to Proterozoic melt depletion events, but that melt-refertilization processes have also been pervasive both during Wilson cycles and during impingement of hotspot magmas. In turn, such processing of mantle may lead to fractionation of inter-element ratios presumed to be otherwise unaffected by melt–rock reaction (e.g. Ru/Ir), and may obscure the true extent of lithospheric melt depletion.

CONCLUSIONS

Aitutaki xenoliths represent oceanic lithosphere that has been entrained by low-degree partial melts from an enriched mantle source. Some pyroxenite xenoliths directly formed from melts whereas some of the pyroxenites and the olivine websterite experienced extensive melt–rock reaction affecting bulk-rock composition. In contrast, spinel lherzolites, harzburgites and dunites are similar in composition to abyssal peridotites with respect to their $^{187}Os/^{188}Os$ ratios (0·1264 ± 82), HSE (Σ_{HSE} = 8–28 ppb) and major element abundances, forsterite contents ($Fo_{89·9\pm1·2}$), and estimated extents of melt depletion (<10 to >15%), and are interpreted to sample relatively shallow Pacific mantle lithosphere that has experienced minimal melt–rock reaction. There is permissible petrological evidence that some peridotites may originate from the garnet stability field, which may have resulted from incorporation of asthenospheric mantle within the aging and thickening Pacific plate. Shallow Pacific mantle lithosphere probably experienced melting during ridge processes at ~100 Ma, and prior melt depletion is evident from Mesoproterozoic to Neoproterozoic depletion ages preserved by some peridotite xenoliths. The variable timing and extent of mantle depletion preserved by the peridotites is superimposed by extensive and recent melt–rock reaction at Aitutaki, occurring during hotspot magmatism, and this process probably affected HSE inter-element ratios (e.g. Pd/Pt, Ru/Ir) and low Os/Ir, but not $^{187}Os/^{188}Os$. Melt depletion ages implied by $^{187}Os/^{188}Os$ measurements of the Aitutaki peridotites are at least >1·5 Ga. Paleoproterozoic (~2 Ga) to recent melt depletion ages are also preserved by xenoliths from the islands of O'ahu (Hawaii), Savai'i (Samoa) and Tubuai (Austral Islands), and by global abyssal peridotites.

Downloaded from https://academic.oup.com/petrology/article/60/9/1753/5613188 by UCSD-Philosophy user on 11 July 2024

These observations indicate that Pacific mantle lithosphere is typical of oceanic lithosphere in general, and that this lithosphere is composed of peridotites that have experienced both recent melt depletion at ridges and prior and sometimes extensive melt depletion across several Wilson cycles.

ACKNOWLEDGEMENTS

Constructive and thoughtful reviews by M. Bizimis, A. Luguet and Q. van der Meer are greatly appreciated. We are grateful to Rita Cabral for assistance with sample collection in the field, to the people of the Cook Islands for their hospitality, to the local pigs for keeping us on our toes, and to then Prime Minister, Jim Marurai, for meeting with us and allowing us to collect samples from the Cook Islands. We thank Frank Keutsch and Tim Cavanaugh at Harvard University for access to the Center for Nanoscale Systems and discussions relating to the orthopyroxene–spinel associations.

FUNDING

This work was supported by grants from the National Geographic Society (NGS 8330-07) and the National Science Foundation (EAR-1447130 and EAR-1918322).

SUPPLEMENTARY DATA

Supplementary data are available at *Journal of Petrology* online.

REFERENCES

Afonso, J. C., Ranalli, G. & Fernandez, M. (2007). Density structure and buoyancy of the oceanic lithosphere revisited. *Geophysical Research Letters* **34**, L10302, doi: 10.1029/2007GL029515.

Birck, J. L., Barman, M. R. & Capmas, F. (1997). Re–Os isotopic measurements at the femtomole level in natural samples. *Geostandards and Geoanalytical Research* **21**, 19–27.

Bizimis, M., Griselin, M., Lassiter, J. C., Salters, V. J. & Sen, G. (2007). Ancient recycled mantle lithosphere in the Hawaiian plume: osmium–hafnium isotopic evidence from peridotite mantle xenoliths. *Earth and Planetary Science Letters* **257**, 259–273.

Boyd, F. R. & Mertzman, S. A. (1987). Composition and structure of the Kaapvaal lithosphere, southern Africa. *Magmatic Processes: Physicochemical Principles*. The Geochemical Society, Special Publication **1**, 13–24.

Chauvel, C., McDonough, W., Guille, G., Maury, R. & Duncan, R. (1997). Contrasting old and young volcanism in Rurutu Island, Austral chain. *Chemical Geology* **139**, 125–143.

Calmant, S., Francheteau, J. & Cazenave, A. (1990). Elastic layer thickening with age of the oceanic lithosphere: a tool for prediction of the age of volcanoes or oceanic crust. *Geophysical Journal International* **100**, 59–67.

Clouard, V. & Gerbault, M. (2008). Break-up spots: could the Pacific open as a consequence of plate kinematics? *Earth and Planetary Science Letters* **265**, 195–208.

Cohen, A. S. & Waters, F. G. (1996). Separation of osmium from geological materials by solvent extraction for analysis by thermal ionisation mass spectrometry. *Analytica Chimica Acta* **332**, 269–275.

Dalrymple, G. B., Jarrard, R. D. & Clague, D. A. (1975). K–Ar ages of some volcanic rocks from the Cook and Austral Islands. *Geological Society of America Bulletin* **86**, 1463–1467.

Day, J. M. D. (2013). Hotspot volcanism and highly siderophile elements. *Chemical Geology* **341**, 50–74.

Day, J. M. D., Pearson, D. G., Macpherson, C. G., Lowry, D. & Carracedo, J. C. (2010). Evidence for distinct proportions of subducted oceanic crust and lithosphere in HIMU-type mantle beneath El Hierro and La Palma, Canary Islands. *Geochimica et Cosmochimica Acta* **74**, 6565–6589.

Day, J. M. D., Peters, B. J. & Janney, P. E. (2014). Oxygen isotope systematics of South African olivine melilitites and implications for HIMU mantle reservoirs. *Lithos* **202**, 76–84.

Day, J. M. D., Waters, C. L., Schaefer, B. F., Walker, R. J. & Turner, S. (2016). Use of hydrofluoric acid desilicification in the determination of highly siderophile element abundances and Re–Pt–Os isotope systematics in mafic–ultramafic rocks. *Geostandards and Geoanalytical Research* **40**, 49–65.

Day, J. M. D., Walker, R. J. & Warren, J. M. (2017). ^{186}Os–^{187}Os and highly siderophile element abundance systematics of the mantle revealed by abyssal peridotites and Os-rich alloys. *Geochimica et Cosmochimica Acta* **200**, 232–254.

Day, J. M. D., Harvey, R. P. & Hilton, D. R. (2019). Melt-modified lithosphere beneath Ross Island and its role in the tectono-magmatic evolution of the West Antarctic Rift System. *Chemical Geology* **518**, 45.

Donnelly, K. E., Goldstein, S. L., Langmuir, C. H. & Spiegelman, M. (2004). Origin of enriched ocean ridge basalts and implications for mantle dynamics. *Earth and Planetary Science Letters* **226**, 347–366.

Fodor, R. V., Bauer, G. R. & Keil, K. (1982). Ultramafic inclusions and megacrysts in olivine nephelinite, Aitutaki Island, Cook Islands. *New Zealand Journal of Geology and Geophysics* **25**, 67–76.

Gannoun, A., Burton, K. W., Day, J. M. D., Harvey, J., Schiano, P. & Parkinson, I. (2016). Highly siderophile element and Os isotope systematics of volcanic rocks at divergent and convergent plate boundaries and in intraplate settings. In: Harvey, J. and Day, J. M. (eds) *Highly Siderophile and Strongly Chalcophile Elements. Mineralogical Society of America and Geochemical Society, Reviews in Mineralogy and Geochemistry* **81**, 651–724.

Hart, S. R. (1984). A large-scale isotope anomaly in the Southern Hemisphere mantle. *Nature* **309**, 753–757.

Hart, S. R., Hauri, E. H., Oschmann, L. A. & Whitehead, J. A. (1992). Mantle plumes and entrainment: isotopic evidence. *Science* **256**, 517–520.

Harvey, J., Gannoun, A., Burton, K. W., Rogers, N. W., Alard, O. & Parkinson, I. J. (2006). Ancient melt extraction from the oceanic upper mantle revealed by Re–Os isotopes in abyssal peridotites from the Mid-Atlantic ridge. *Earth and Planetary Science Letters* **244**, 606–621.

Hauri, E. H., Shimizu, N., Dieu, J. J. & Hart, S. R. (1993). Evidence for hotspot-related carbonatite metasomatism in the oceanic upper mantle. *Nature* **365**, 221–227.

Hirth, G. & Kohlstedt, D. L. (1996). Water in the oceanic upper mantle: implications for rheology, melt extraction and the evolution of the lithosphere. *Earth and Planetary Science Letters* **144**, 93–108.

Hofmann, A. W. (1997). Mantle geochemistry: the message from oceanic volcanism. *Nature* **385**, 219–229.

Ireland, T. J., Walker, R. J. & Garcia, M. O. (2009). Highly siderophile element and ^{187}Os isotope systematics of Hawaiian picrites: implications for parental melt composition and source heterogeneity. *Chemical Geology* **260**, 112–128.

Downloaded from https://academic.oup.com/petrology/article/60/9/1753/5613188 by UCSD-Philosophy user on 11 July 2024

Ishikawa, A., Pearson, D. G. & Dale, C. W. (2011). Ancient Os isotope signatures from the Ontong Java Plateau lithosphere: Tracing lithospheric accretion history. *Earth and Planetary Science Letters* **301**, 159–170.

Jackson, M. G., Shirey, S. B., Hauri, E. H., Kurz, M. D. & Rizo, H. (2016). Peridotite xenoliths from the Polynesian Austral and Samoa hotspots: Implications for the destruction of ancient ^{187}Os and ^{142}Nd isotopic domains and the preservation of Hadean ^{129}Xe in the modern convecting mantle. *Geochimica et Cosmochimica Acta* **185**, 21–43.

Jackson, M. G., Halldorsson, S. A., Price, A., Kurz, M. D., Konter, J. G., Koppers, A. A. P. & Day, J. M. D. (2019). Contrasting old and young volcanism from Aitutaki, Cook Islands: Evidence for a distinct Rarotonga hotspot? *Goldschmidt Conference, 2019, White Iron*.

Johnson, K., Dick, H. J. & Shimizu, N. (1990). Melting in the oceanic upper mantle: an ion microprobe study of diopsides in abyssal peridotites. *Journal of Geophysical Research* **95**, 2661–2678.

Karato, S. I. (1986). Does partial melting reduce the creep strength of the upper mantle? *Nature* **319**, 309–310.

Kelemen, P. B., Dick, H. J. & Quick, J. E. (1992). Formation of harzburgite by pervasive melt/rock reaction in the upper mantle. *Nature* **358**, 635–641.

Lassiter, J. C., Byerly, B. L., Snow, J. E. & Hellebrand, E. (2014). Constraints from Os-isotope variations on the origin of Lena Trough abyssal peridotites and implications for the composition and evolution of the depleted upper mantle. *Earth and Planetary Science Letters* **403**, 178–187.

Lissenberg, C. J. & Dick, H. J. (2008). Melt–rock reaction in the lower oceanic crust and its implications for the genesis of mid-ocean ridge basalt. *Earth and Planetary Science Letters* **271**, 311–325.

Lorand, J. P. & Luguet, A. (2016). Chalcophile and siderophile elements in mantle rocks: trace elements controlled by trace minerals. In: Harvey, J. and Day, J. M. (eds) *Highly Siderophile and Strongly Chalcophile Elements. Mineralogical Society of America and Geochemical Society, Reviews in Mineralogy and Geochemistry* **81**, 441–488.

Luguet, A. & Reisberg, L. (2016). Highly siderophile element and ^{187}Os signatures in non-cratonic basalt-hosted peridotite xenoliths: Unravelling the origin and evolution of the post-Archean lithospheric mantle. In: Harvey, J. and Day, J. M. (eds) *Highly Siderophile and Strongly Chalcophile Elements. Mineralogical Society of America and Geochemical Society, Reviews in Mineralogy and Geochemistry* **81**, 305–367.

Macgregor, I. D. (1974). The system MgO–Al_2O_3–SiO_2: solubility of Al_2O_3 in enstatite for spinel and garnet peridotite compositions. *American Mineralogist* **59**, 110–119.

Manga, M. (1996). Mixing of heterogeneities in the mantle: effect of viscosity differences. *Geophysical Research Letters* **23**, 403–406.

McDonough, W. F. & Sun, S. S. (1995). The composition of the Earth. *Chemical Geology* **120**, 223–253.

McKenzie, D. & O'Nions, R. K. (1991). Partial melt distributions from inversion of rare earth element concentrations. *Journal of Petrology* **32**, 1021–1091.

Meisel, T. & Horan, M. F. (2016). Analytical methods for the highly siderophile elements. In: Harvey, J. and Day, J. M. (eds) *Highly Siderophile and Strongly Chalcophile Elements. Mineralogical Society of America and Geochemical Society, Reviews in Mineralogy and Geochemistry* **81**, 89–106.

Meisel, T., Walker, R. J., Irving, A. J. & Lorand, J. P. (2001). Osmium isotopic compositions of mantle xenoliths: a global perspective. *Geochimica et Cosmochimica Acta* **65**, 1311–1323.

Morgan, W. J. (1972). Deep mantle convection plumes and plate motions. *AAPG Bulletin* **56**, 203–213.

Müller, R. D., Sdrolias, M., Gaina, C. & Roest, W. R. (2008). Age, spreading rates, and spreading asymmetry of the world's ocean crust. *Geochemistry, Geophysics, Geosystems* **9**, Q04006,

Nakamura, Y. & Tatsumoto, M. (1988). Pb, Nd, and Sr isotopic evidence for a multicomponent source for rocks of Cook–Austral Islands and heterogeneities of mantle plumes. *Geochimica et Cosmochimica Acta* **52**, 2909–2924.

Nimis, P. & Grütter, H. (2010). Internally consistent geothermometers for garnet peridotites and pyroxenites. *Contributions to Mineralogy and Petrology* **159**, 411–427.

Niu, Y. (2004). Bulk-rock major and trace element compositions of abyssal peridotites: implications for mantle melting, melt extraction and post-melting processes beneath mid-ocean ridges. *Journal of Petrology* **45**, 2423–2458.

Obata, M. (2011). Kelyphite and symplectite: textural and mineralogical diversities and universality, and a new dynamic view of their structural formation. In: *New Frontiers in Tectonic Research—General Problems, Sedimentary Basins and Island Arcs*. London: IntechOpen, pp. 93–122.

O'Driscoll, B., Day, J. M. D., Walker, R. J., Daly, J. S., McDonough, W. F. & Piccoli, P. M. (2012). Chemical heterogeneity in the upper mantle recorded by peridotites and chromitites from the Shetland Ophiolite Complex, Scotland. *Earth and Planetary Science Letters* **333**, 226–237.

O'Driscoll, B., Walker, R. J., Clay, P. L., Day, J. M. D., Ash, R. D. & Daly, J. S. (2018). Length-scales of chemical and isotopic heterogeneity in the mantle section of the Shetland Ophiolite Complex, Scotland. *Earth and Planetary Science Letters* **488**, 144–154.

Ritzwoller, M. H., Shapiro, N. M. & Zhong, S.-J. (2004). Cooling history of the Pacific lithosphere. *Earth and Planetary Science Letters* **226**, 69–84.

Rose, J. & Koppers, A. A. P. (2019). Simplifying age progressions within the Cook–Austral Islands using high-resolution ARGUS-VI ^{40}Ar/^{39}Ar incremental heating ages. *Geochemistry, Geophysics, Geosystems*, doi: 10.1029/2019GC008302.

Sandwell, D. T. & Smith, W. H. F. (2009). Global marine gravity from retracked Geosat and ERS-1 altimetry: ridge segmentation versus spreading rate. *Journal of Geophysical Research* **114**, B01411, doi:10.1029/2008JB006008.

Schiano, P., Burton, K. W., Dupré, B., Birck, J. L., Guille, G. & Allègre, C. J. (2001). Correlated Os–Pb–Nd–Sr isotopes in the Austral–Cook chain basalts: the nature of mantle components in plume sources. *Earth and Planetary Science Letters* **186**, 527–537.

Sclater, J. G. & Francheteau, J. (1970). The implications of terrestrial heat flow observations on current tectonic and geochemical models of the crust and upper mantle of the Earth. *Geophysical Journal International* **20**, 509–542.

Scott, J. M., Waight, T. E., Van der Meer, Q. H. A., Palin, J. M., Cooper, A. F. & Münker, C. (2014). Metasomatized ancient lithospheric mantle beneath the young Zealandia microcontinent and its role in HIMU-like intraplate magmatism. *Geochemistry, Geophysics, Geosystems* **15**, 3477–3501.

Simon, N. S., Neumann, E. R., Bonadiman, C., Coltorti, M., Delpech, G., Grégoire, M. & Widom, E. (2008). Ultra-refractory domains in the oceanic mantle lithosphere sampled as mantle xenoliths at ocean islands. *Journal of Petrology* **49**, 1223–1251.

Downloaded from https://academic.oup.com/petrology/article/60/9/1753/5613188 by UCSD-Philosophy user on 11 July 2024

Sleep, N. H. (2002). Ridge-crossing mantle plumes and gaps in tracks. *Geochemistry, Geophysics, Geosystems* **3**, 1–33.

Smith, D. (1977). The origin and interpretation of spinel–pyroxene clusters in peridotite. *Journal of Geology* **85**, 476–482.

Spacek, P., Ackerman, L., Habler, G., Abart, R. & Ulrych, J. (2013). Garnet breakdown, symplectite formation and melting in basanite-hosted peridotite xenoliths from Zinst (Bavaria, Bohemian Massif). *Journal of Petrology* **54**, 1691–1723.

Suhr, G., Seck, H. A., Shimizu, N., Günther, D. & Jenner, G. (1998). Infiltration of refractory melts into the lowermost oceanic crust: evidence from dunite- and gabbro-hosted clinopyroxenes in the Bay of Islands Ophiolite. *Contributions to Mineralogy and Petrology* **131**, 136–154.

Sun, C. & Liang, Y. (2014). An assessment of subsolidus re-equilibration on REE distribution among mantle minerals olivine, orthopyroxene, clinopyroxene, and garnet in peridotites. *Chemical Geology* **372**, 80–91.

Sun, S. S. & McDonough, W. S. (1989). Chemical and isotopic systematics of oceanic basalts: implications for mantle composition and processes. In: Saunders, A. D. and Norry, M. J. (eds) *Magmatism in the Ocean Basins. Geological Society, London, Special Publications* **42**, 313–345.

Turner, D. L. & Jarrard, R. D. (1982). K–Ar dating of the Cook–Austral island chain: a test of the hot-spot hypothesis. *Journal of Volcanology and Geothermal Research* **12**, 187–220.

van der Meer, Q. H., Klaver, M., Reisberg, L., Riches, A. J. & Davies, G. R. (2017). Preservation of an Archaean whole rock Re–Os isochron for the Venetia lithospheric mantle: Evidence for rapid crustal recycling and lithosphere stabilisation at 3·3 Ga. *Geochimica et Cosmochimica Acta* **216**, 242–263.

Warren, J. M. (2016). Global variations in abyssal peridotite compositions. *Lithos* **248**, 193–219.

White, R. W. (1966). Ultramafic inclusions in basaltic rocks from Hawaii. *Contributions to Mineralogy and Petrology* **12**, 245–314.

Wood, B. L. (1967). Geology of the Cook Islands. *New Zealand Journal of Geology and Geophysics* **10**, 1429–1445.

Wood, C. P. (1978). Petrology of Aitutaki, Cook Islands (Note). *New Zealand Journal of Geology and Geophysics* **21**, 761–765.

Workman, R. K. & Hart, S. R. (2005). Major and trace element composition of the depleted MORB mantle (DMM). *Earth and Planetary Science Letters* **231**, 53–72.

Wright, E. (1987). Mineralogical studies of Samoan ultramafic xenoliths: implications for upper mantle processes. In: Keating, B. H., Fryer, P., Batiza, R. and Boehlert, G. W. (eds) *Seamounts, Islands, and Atolls. American Geophysical Union, Geophysical Monograph*, **43**, 221–233.

Zhong, J. Q. & Zhang, J. (2005). Thermal convection with a freely moving top boundary. *Physics of Fluids* **17**, 115105.

Zhou, M.-F., Robinson, P. T., Malpas, J. & Li, Z. (1996). Podiform chromitites in the Luobusa Ophiolite (Southern Tibet): implications for melt–rock interaction and chromite segregation in the upper mantle. *Journal of Petrology* **37**, 3–21.

Zindler, A. & Hart, S. (1986). Chemical geodynamics. *Annual Review of Earth and Planetary Sciences* **14**, 493–571.

Downloaded from https://academic.oup.com/petrology/article/60/9/1753/5613188 by UCSD-Philosophy user on 11 July 2024

Deltech Furnaces

Sustained operating temperatures to 1800° Celsius

www.deltechfurnaces.com

Gas Mixing System

An ISO 9001:2015 certified company

Custom Vertical Tube

ASME NQA-1 2008 Nuclear Quality Assurance

Standard Vertical Tube

Control systems are certified by Intertek UL508A compliant

Bottom Loading Vertical Tube